Robust Solar Sail Trajectory Design under Uncertainty with Application to NEA Scout Mission

Kenshiro Oguri [*], Gregory Lantoine [†], and Theodore H. Sweetser [‡]
Jet Propulsion Laboratory, California Institute of Technology, Pasadena, California 91109

Solar sailing is an emerging technology that harnesses solar radiation pressure to propel spacecraft, providing the potential to enable longer-duration, higher Delta-V missions. To ensure successful solar sailing missions, mission designers need to design trajectories that are robust against uncertainty due to navigation error, control error, and unplanned transition to the safe mode. Based on deterministic and stochastic approaches, this study develops frameworks that design robust solar sailing trajectories under such uncertainty. The developed frameworks are applied to the NEA Scout mission, a NASA's CubeSat solar sailing asteroid exploration mission onboard Artemis I.

I. Introduction

Solar sailing has the potential to enable longer-duration, higher Delta-V missions compared to conventional missions with chemical or electric propulsion. Harnessing solar radiation pressure (SRP) to propel spacecraft, it does not consume propellant as the primary means of its orbit control. This propellant-free orbit control capability is particularly beneficial for small spacecraft with limited launch mass, providing them with opportunities to travel interplanetary space without relying on conventional propulsion systems. The technology of solar sailing has been recently demonstrated in orbit by JAXA's IKAROS (2010) [1], NASA's NanoSail-D2 (2010) [2], and The Planetary Society's LightSail 1 and 2 (2015, 2019) [3]. Given these successful demonstrations, the maturing technology of solar sailing is being considered as a practical option for interplanetary travel. Indeed, space agencies plan or propose multiple sail-based space exploration missions in the 2020s, such as NASA's NEA Scout for near-Earth asteroid (NEA) exploration [4], NASA's Solar Cruiser for heliophysics [5], and JAXA's OKEANOS for Jupiter Trojan asteroid exploration [6].

Like any other space missions, designing optimal trajectories is fundamental in solar sail mission design. Since NASA's Jet Propulsion Laboratory (JPL) initiated the feasibility assessment of solar sailing missions for rendezvous with comet Halley in the 1970s, the art of solar-sail trajectory optimization has been greatly advanced by many studies, including early studies assuming idealized sail models [7, 8] and recent studies with realistic mission scenarios and/or practical assumptions, based on direct approaches (e.g., Refs. 9, 10) and indirect approaches (e.g., Refs. 11, 12).

At the same time, any space trajectories are subject to uncertain errors due to various causes. To ensure successful solar sailing missions, mission designers need to design trajectories that are robust against possible errors. Such uncertain errors can be categorized into two types: state uncertainty and occurrence of undesirable events such as unplanned transition to the safe mode. The state uncertainty is induced by multiple sources, such as uncertain errors in the SRP force model, attitude control, and orbit determination (OD) solutions. Under such state uncertainty, sailcraft has to perform trajectory correction maneuvers (TCMs) to maintain its trajectory close to the reference. Likewise, the occurrence of an unplanned safe-mode event leads to the necessity to replan the sail trajectory after recovery, as the sail attitude cannot be freely controlled during a safe mode, introducing off-nominal acceleration. Either case, it is crucial that sail trajectories be designed robust to such uncertainties, providing missions with enough mission margins for TCMs and recoveries.

The goal of this study is to develop frameworks that design robust solar sailing trajectories under uncertainty. In the context of low-thrust trajectory optimization, an increasing number of approaches based on stochastic optimal control have been recently proposed, including [13–16], producing initial yet promising results of the use of stochastic optimal control for trajectory optimization under uncertainty (see Introduction of Ref. 16 for a literature review on this topic with more details). Designing robust solar sailing trajectories can be even more challenging because of the less orbit control authority of SRP-based orbit control, due to the asymmetric acceleration controllability (SRP acceleration cannot be

---

[*]JPL Postdoctoral Fellow, Mission Design and Navigation Section. Member AIAA.
[†]Mission Design Engineer, Mission Design and Navigation Section. Member AIAA.
[‡]Mission Design Engineer, Mission Design and Navigation Section. Senior Member AIAA.
©2022 California Institute of Technology. Government sponsorship acknowledged.
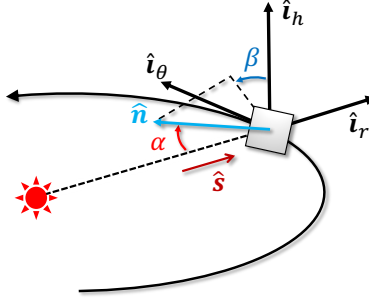
Figure 1   Heliocentric orbit frame $O\{\hat{i}_r, \hat{i}_\theta, \hat{i}_h\}$ and sail attitude representation via α and β

oriented toward the Sun) and to the coupling between the acceleration direction and magnitude. There are a handful of studies on this problem, such as designing conservative trajectories by shedding excess thrust to accommodate pre-launch modeling errors [17], solving stochastic optimal control problems via differential dynamic programming with unscented transform [18], and incorporating expected angle fraction as a margin in the trajectory design process [19].

In this study, two distinct approaches, deterministic and stochastic approaches, are taken to address the problem of designing robust solar sailing trajectories. In the deterministic approach, two candidate mission margins are first identified by backward reachability analysis of solar sailing trajectories (Section IV), and a solution method is developed to incorporate these margin quantities in the reference trajectory design process (Section V). The stochastic approach develops a solution method based on stochastic optimal control and sequential convex programming to design robust reference trajectories that satisfy probabilistic constraints under navigation and control errors (Section VI). These developed methods are applied to the interplanetary cruise phase of the NEA Scout mission design, demonstrating their effectiveness and current limitations to be further improved.

II. Dynamics

A. Solar Radiation Pressure

This study models the acceleration caused by solar radiation pressure (SRP) by using the optical force model [20]. The simple mathematical expression allows us to derive closed-form expressions of the optimal control law for orbit transfers while the flexibility of the model captures major contributions of SRP by taking into account the specular reflection, diffusive reflection, absorption, and re-radiation of photon.

Based on the optical force model, SRP acceleration, $\boldsymbol{a}_s \in \mathbb{R}^3$, is expressed as follows (see Ref. 12 for the derivation):

$$\boldsymbol{a}_s = -\frac{\sigma G_0}{d^2} \hat{\boldsymbol{n}}^\top \hat{\boldsymbol{s}} \left[(C_1 \hat{\boldsymbol{n}}^\top \hat{\boldsymbol{s}} - C_2) \hat{\boldsymbol{n}} + C_3 \hat{\boldsymbol{s}} \right], \tag{1}$$

where $G_0 (\approx 1.02 \times 10^{14}~\text{kg} \cdot \text{km/s}^2)$ is the solar flux constant at the Earth, d is the Sun-spacecraft distance, and $\sigma = A/m$ [km^2/kg] denotes the area-to-mass ratio of a flat sail of area A and mass m. $\hat{\boldsymbol{s}} \in \mathbb{R}^3$ and $\hat{\boldsymbol{n}} \in \mathbb{R}^3$ represent unit vectors aligned with the sunlight and sail normal, respectively. The three coefficients, C_1, C_2, and C_3, represent a minimal set of the SRP coefficients that encapsulate sail surface properties such as the total reflectivity, specular and diffusive reflections, and surface emissivity, defined in Ref. 12.

Next, consider expressing the SRP acceleration Eq. (1) in a vector component form. Define a heliocentric orbit frame $O\{\hat{i}_r, \hat{i}_\theta, \hat{i}_h\}$ with its origin at the center of the mass of the Sun, where $\hat{i}_r$ is along the heliocentric orbit radius vector, $\hat{i}_h$ is along the heliocentric orbit angular momentum vector, and $\hat{i}_\theta$ completes the right-hand system. Then $\hat{\boldsymbol{n}}$ and $\hat{\boldsymbol{s}}$ are expressed in the orbit frame O as (using a left superscript to denote the reference frame):

$$^O\hat{\boldsymbol{n}} = \begin{bmatrix} -\cos\alpha & \sin\alpha\sin\beta & \sin\alpha\cos\beta \end{bmatrix}^\top, \quad ^O\hat{\boldsymbol{s}} = \begin{bmatrix} 1 & 0 & 0 \end{bmatrix}^\top, \tag{2}$$

where $\hat{\boldsymbol{n}}$ is parameterized by the sail attitude angles α and β; α represents the cone angle of the sail normal with respect to the sunlight while β is the clock angle of the sail normal around $\hat{i}_r$. α is also called sunlight incident angle or simply solar angle. Fig. 1 illustrates the orbit frame O and the attitude angles α and β along with $\hat{\boldsymbol{n}}$ and $\hat{\boldsymbol{s}}$. Thus, Eq. (1) is

expressed in the orbit frame O as:

$$
{}^{O}\boldsymbol{a}_s = \frac{\sigma G_0}{d^2} \cos \alpha \begin{bmatrix} C_1 \cos^2 \alpha + C_2 \cos \alpha + C_3 \\ -(C_1 \cos \alpha + C_2) \sin \alpha \sin \beta \\ -(C_1 \cos \alpha + C_2) \sin \alpha \cos \beta \end{bmatrix}.
\tag{3}
$$

This study assumes that α has a maximum constraint, i.e., $0 \leq \alpha \leq \alpha_{\max} \leq \pi/2$, while no constraint is assumed for β. Imposing constraints on α is crucial when considering practical applications; for instance, imposing $\alpha \leq \alpha_{\max}$ is often necessary to ensure sufficient power generation.

B. Equations of Motion

Let $\boldsymbol{x} \in \mathbb{R}^{n_x}$, $\boldsymbol{a} \in \mathbb{R}^3$, and $\boldsymbol{u} \in \mathbb{R}^{n_u}$ be the orbital state, acceleration (including SRP and other perturbations), and control input, respectively. Since this study considers solar sailing as our orbital control, the sail attitude angles α and β are taken as the control input, i.e., $\boldsymbol{u} \triangleq [\alpha, \beta]^\top \in \mathcal{U}$, where the domain of $\boldsymbol{u}$, $\mathcal{U}$, is expressed as:

$$
\mathcal{U} = \left\{ [\alpha, \beta]^\top \mid 0 \leq \alpha \leq \alpha_{\max} \leq \pi/2, \ -\pi \leq \beta \leq \pi \right\}.
\tag{4}
$$

The total acceleration $\boldsymbol{a}$ is expressed as $\boldsymbol{a}(\boldsymbol{x}, \boldsymbol{u}, t) = \boldsymbol{a}_d(\boldsymbol{x}, t) + \boldsymbol{a}_s(\boldsymbol{x}, \boldsymbol{u})$, where $\boldsymbol{a}_d$ is the sum of disturbing acceleration except SRP. The orbital dynamics can then be expressed in the following generic form:

$$
\dot{\boldsymbol{x}} = \boldsymbol{f}(\boldsymbol{x}, \boldsymbol{u}, t) = \boldsymbol{f}_0(\boldsymbol{x}, t) + F(\boldsymbol{x})\boldsymbol{a}_s(\boldsymbol{x}, \boldsymbol{u}, t),
\tag{5}
$$

where $\boldsymbol{f}_0(\cdot)$ and $F(\cdot)$ represent the perturbed two-body dynamics and the control influence matrix, respectively; $\boldsymbol{f}_0(\cdot)$ can be also expressed as a combination of the Keplerian dynamics and the contribution of non-SRP perturbations as:

$$
\boldsymbol{f}_0(\boldsymbol{x}, t) = \boldsymbol{f}_{\text{kep}}(\boldsymbol{x}) + F(\boldsymbol{x})\boldsymbol{a}_d(\boldsymbol{x}, t).
\tag{6}
$$

The generic form in Eq. (5) encompasses equations of motion in various coordinate systems. Two specific forms, one in the modified equinoctial coordinates and another in the Cartesian coordinates are considered in this paper and presented in Sections II.B.1 and II.B.2, respectively.

1. Equations of Motion in Modified Equinoctial Coordinates

In an orbital element coordinate system, $F(\cdot)$ in Eq. (5) represents the stacked Gauss variational equations, whose specific expression depends on the choice of the orbital elements. Among various sets of orbital elements, modified equinoctial orbital elements (MEEs) [21] are known for the numerical advantages, including the slow variations of five out of six elements under perturbations and the non-singular behavior except at 180-degree inclination. In MEE coordinates, the state vector $\boldsymbol{x}$ is expressed as:

$$
\boldsymbol{x} = \begin{bmatrix} p & f & g & h & k & L \end{bmatrix}^\top,
\tag{7}
$$

where L is the true longitude. Each element is defined by using the Keplerian orbital elements $\{a, e, i, \Omega, \omega, \nu\}$ (ν: true anomaly) as follows:

$$
p = a(1 - e^2), \ \ h = \tan\frac{i}{2}\cos\Omega, \ \ f = e\cos(\omega + \Omega), \ \ k = \tan\frac{i}{2}\sin\Omega, \ \ g = e\sin(\omega + \Omega), \ \ L = \nu + \omega + \Omega.
\tag{8}
$$

$\boldsymbol{f}_{\text{kep}}(\cdot)$ and $F(\cdot)$ for the MEE coordinates can be found in literature (e.g., Ref. 21; Ref. 12 for its vector-matrix form). The columns of $F(\cdot)$ are associated with acceleration expressed in the radial, transverse, and normal (RTN) frame, which corresponds to our orbit frame (O-frame) introduced in Section II.A. We can therefore compute the contribution of SRP acceleration to the state variation by simply multiplying $F(\cdot)$ and ${}^{O}\boldsymbol{a}_s$ as $F{}^{O}\boldsymbol{a}_s$.

2. Equations of Motion in Cartesian coordinates

In the Cartesian coordinates, the state vector typically consists of the spacecraft position ($\boldsymbol{r} \in \mathbb{R}^3$) and velocity ($\boldsymbol{v} \in \mathbb{R}^3$), i.e., $\boldsymbol{x} = [\boldsymbol{r}^\top, \boldsymbol{v}^\top]^\top$. Denoting by $\mathcal{I}\{\hat{\boldsymbol{i}}_x, \hat{\boldsymbol{i}}_y, \hat{\boldsymbol{i}}_z\}$ the inertial frame in which $\boldsymbol{x}$ is defined, $\boldsymbol{f}_0$ and F are simply

$$
\boldsymbol{f}_0({}^{\mathcal{I}}\boldsymbol{x}) = \begin{bmatrix} {}^{\mathcal{I}}\boldsymbol{v} \\ -\frac{\mu}{\|\boldsymbol{r}\|_2^3}{}^{\mathcal{I}}\boldsymbol{r} \end{bmatrix}, \quad F = \begin{bmatrix} 0_{3\times3} \\ I_3 \end{bmatrix},
\tag{9}
$$

3

(a) Asteroid observation during slow flyby
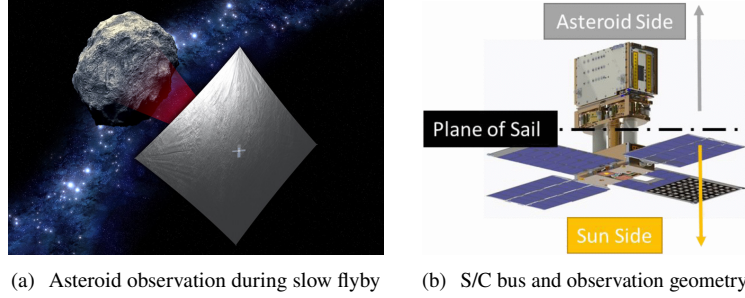

(b) S/C bus and observation geometry

Figure 2   NEA Scout images [4]

where μ is the gravitational parameter of the primary body. The columns of F are associated with the $\mathcal{I}$-frame. In other words, $^O\boldsymbol{a}_s$ needs to be converted to $^{\mathcal{I}}\boldsymbol{a}_s$ when calculating the state variation due to $\boldsymbol{a}_s$, i.e., $F\,^{\mathcal{I}}\mathbf{C}_O(\boldsymbol{x})^O\boldsymbol{a}_s$, where $^{\mathcal{I}}\mathbf{C}_O(\boldsymbol{x})$ denotes a transformation matrix that maps a vector in the O-frame to the $\mathcal{I}$-frame. Denoting the unit vectors of $\boldsymbol{r}$ and $\boldsymbol{h}(=\boldsymbol{r}\times\boldsymbol{v})$ by $\hat{\boldsymbol{r}}$ and $\hat{\boldsymbol{h}}$, $^{\mathcal{I}}\mathbf{C}_O(\boldsymbol{x})$ is given by

$$^{\mathcal{I}}\mathbf{C}_O(\boldsymbol{x}) = \begin{bmatrix} ^{\mathcal{I}}\hat{\boldsymbol{r}} & ^{\mathcal{I}}\hat{\boldsymbol{h}} \times {}^{\mathcal{I}}\hat{\boldsymbol{r}} & ^{\mathcal{I}}\hat{\boldsymbol{h}} \end{bmatrix} \tag{10}$$

III. NEA Scout Mission

A. Overview

The NEA Scout mission is a reconnaissance mission to investigate a small NEA during a slow flyby. This mission is jointly developed by NASA's Marshall Space Flight Center (MSFC) and JPL, sponsored by the Advanced Exploration Systems Division of the Human Exploration and Operations Mission Directorate. The NEA Scout spacecraft, shown in Fig. 2, is a 6U CubeSat with sail area of 86 m^2, onboard NASA's Artemis I. The characteristic parameters of the sailcraft used in this study are the same as those used in Ref. 12. See Ref. 4 for more detail of the mission.

The orbit transfer to the target NEA leverages its solar sailing propulsion and consists of the following phases: launch, cislunar escape, interplanetary cruise, detection & approach, and data downlink. This paper is focused on the mission design of the interplanetary cruise phase.

B. Interplanetary Cruise Phase

The interplanetary cruise phase begins with departure from the cislunar space and completes with rendezvous with a target asteroid (precisely speaking, the rendezvous point is set slightly sunward of the asteroid to accommodate the approach phase in the actual mission implementation). In this study, the reference trajectories are designed with the epoch of cislunar departure on October 1st 2022, and 2020 GE is chosen as the target asteroid. The Keplerian elements of 2020 GE at the epoch of cislunar departure are: $\{a, e, i, \omega, \Omega, \nu_{sb0}\} = \{1.007\,\text{AU}, 0.039, 0.040\,\text{rad}, 1.850\,\text{rad}, 3.146\,\text{rad}, 1.523\,\text{rad}\}$, where ν_{sb0} denotes the asteroid true anomaly. As the transfer trajectory to 2020 GE remains in the vicinity of the Earth, the trajectory is subject to significant influence of the Earth gravity. This influence is taken into account in the dynamical model assumed in this study as a third-body perturbation, incorporated as $\boldsymbol{a}_d(\boldsymbol{x}, t)$ in Eq. (6).

IV. Mission Margins in Solar Sailing

A. Margins in Trajectory Design

Let us first discuss necessary properties for a quantity to be qualified as a mission margin in a general space mission design context, which helps guide us to identify margin quantities for solar sailing trajectories. The first property we would expect is *robustness*; it is natural to expect that incorporating a margin in the mission design process improve the robustness of trajectories against possible errors. Another property would be *achievability*; in order for trajectories designed with a margin quantity is meaningful, such trajectories should be implementable, i.e., physically achievable, in reality.
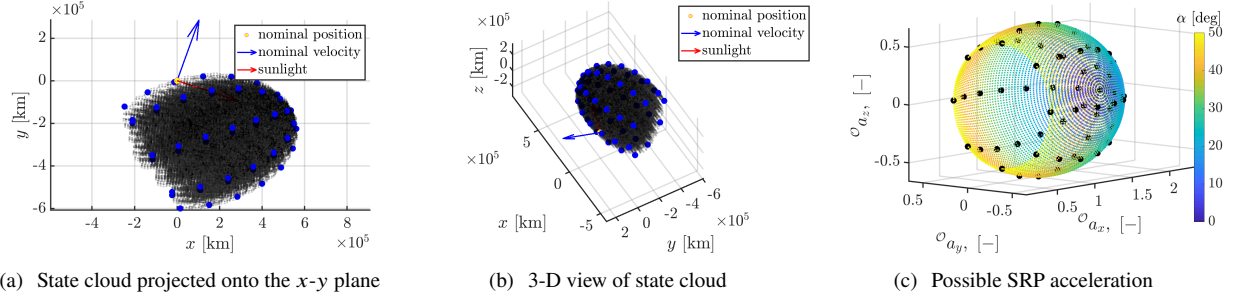
4

(a) State cloud projected onto the x-y plane   (b) 3-D view of state cloud   (c) Possible SRP acceleration

Figure 3   **Reachability analysis. (a), (b): Snapshot of the backward reachable set for GE 2020, propagated from t_f to $t = t_f - 63$ [day] (black dots). Blue spheres represent a subset of the reachable set with constant sail attitude. The coordinates are shifted to locate the nominal state at the origin. (c): Possible SRP acceleration with $\alpha_{\max} = 50$ deg (colored dots) and discretization points for reachability analysis (black spheres)**

In conventional low-thrust design, for instance, a quantity called *duty cycle* has been utilized in the mission design process as a margin [22]. The duty cycle is defined as the percent ratio of time being available to operate the engine at the maximum thrust level out of the total transfer time. This quantity indeed satisfies both of the margin qualifications *robustness* and *achievability*; it has been empirically confirmed that incorporating a duty cycle improves the robustness of reference trajectories [23–25], and trajectories designed with this margin can be achieved by having reduced thrusting periods equivalent to the chosen duty cycle on average.

On the other hand, as of now, there is no such margin quantity commonly accepted for solar-sail trajectories. An analogous quantity to the duty cycle could be to use a reduced sail area in the reference trajectory design, although the robustness and achievability of such trajectories are either unknown or questionable. Exploring appropriate margin quantities for solar sailing that satisfy the two requirements is one of the key steps of our deterministic approach.

B. Backward Reachability Analysis

In the process of exploring appropriate margin quantities for solar sailing, backward reachability analysis is performed, where reachable sets of solar-sail trajectories are computed backward in time. Since the sets are computed backward, each set is defined by a cloud of states that can reach the target state in a given amount of time. The primary purposes of this analysis are to investigate and visualize how the reachable set of solar sail trajectories evolve over time and where reference trajectories of our interest are located with respect to the reachable set.

The reachable sets are computed by nonlinearly propagating the orbital state backward in time, starting from the target state (i.e., the state of GE 2020) at a given time t_f, while applying all the possible histories of solar sail acceleration with some discretization in acceleration and time. This study uses a relatively coarse discretization (mainly due to the memory limitation to save the propagated states), where the acceleration domain is discretized into 64, corresponding to 8 different α and 8 different β; the time domain is discretized to have 21-day intervals between each acceleration update. Fig. 3(c) depicts normalized SRP acceleration that corresponds to every pair of $\{\alpha, \beta\}$ with $\alpha \le \alpha_{\max} = 50$, shown in the O-frame, where the discretization points are emphasized as black spheres. Figs. 3(a) and 3(b) show a snapshot of the computed backward reachable sets at $t = t_f - 63$, which therefore contains the propagated states of $(8 \times 8)^3 \sim 262,000$ trajectories. These figures also highlight some states with special meanings: the state propagated with an optimal control profile (yellow sphere; termed *nominal state*), where the control profile in Fig. 4(d) is used for this analysis, and those propagated with constant attitudes (blue spheres), which correspond to each of the 64-discretized sail attitudes.

Fig. 3 reveals three key observations: (i) the nominal state lies on the surface of the reachable set; (ii) the reachable set is filled with the samples (i.e., not hollow) despite the hollow structure of possible SRP acceleration; and (iii) the surface of the reachable set is defined by the samples with constant attitudes. The observation (i) implies an undesirable situation for us in terms of the robustness of the nominal trajectory; that is, even a very small perturbation may push the nominal trajectory outside of the reachable set, meaning that the perturbed trajectory is not able to reach the target at the specified epoch t_f (this does not exclude the possibility of reaching the target at different epochs). Ideally, we would like to design reference trajectories that are inside of the reachable set as much as possible, providing the trajectories with some margins before being pushed out from the set. On the other hand, the observation (ii) brings us good news; the solid interior of the reachable set implies that there are indeed feasible control profiles that place solar sail trajectories

5

inside of the set. If we incorporate such control profiles in our reference trajectory design process, it would improve the robustness of trajectories in the sense that they will be reachable to the target at the specified epoch under some perturbations. Lastly, the observation (iii) facilitates our qualitative understanding of the relationship between locations in the reachable set and control profiles; since each blue sphere in Figs. 3(a) and 3(b) corresponds to each of the black spheres in Fig. 3(c), we can roughly locate where the state would end up in the reachable set for a specific control profile. This provides us with the following insights; a smaller α would move the state toward the "top" of the hat-shaped reachable set, a greater α would shift toward the "bottom," and a moderate α would keep it around the middle. Likewise, β plays a main role in revolving the state along the hat surface, changing SRP acceleration in the $y-z$ direction in the O-frame (i.e., ${}^O a_y$, ${}^O a_z$). These can be also summarized as follows; ${}^O a_x$ would primarily contributes to moving the state in the bottom-top direction of the hat while ${}^O a_y$, ${}^O a_z$ would in the perpendicular direction.

Obviously, the shape of the reachable set and the location of the nominal state would be different for longer propagation. The nominal state and the constant-attitude samples may be located inside the reachable set after longer backward propagation (i.e., at an earlier epoch), which was indeed observed when a ∼300-day backward propagation was performed. It implies that perturbations applied at earlier part of trajectories are less detrimental, which is consistent with our intuition (the latter perturbations are applied, the harder it is to correct trajectories to reach the same target).

C. Candidate Margins in Solar Sail Trajectory Design

Based on the discussion in Section IV.B, this study considers the following quantities as potential promising margins in solar sail trajectory design: (1) moderate cone angle; and (2) reduced $y-z$ acceleration (in the O-frame).

The margin (1) is straightforward from the discussion associated with the observation (iii); the discussion suggests that having a control profile with moderate α would allow the state to remain around the middle in the direction from the bottom to the top of the hat-shaped reachable set. In other words, reference trajectory designed with moderate cone angle over the transfer would have greater robustness. Another requirement for margin quantities, achievability, is automatically satisfied if such reference trajectories are successfully designed.

The idea behind proposing the margin (2) is based on the observations (ii) and (iii). The observation (ii) clarifies that there exist feasible control profiles that place our trajectories inside the feasible set. Furthermore, the discussion based on the observation (iii) identifies that ${}^O a_y$, ${}^O a_z$ would primarily contribute to moving the state in the perpendicular direction, complementing the role played by α. Combining these two observations, we may design reference trajectories that reside in the interior of the reachable set by using reduced $y-z$ acceleration, such as ${}^O \boldsymbol{a}_s = [a_x \ \Gamma a_y \ \Gamma a_z]$ where $\Gamma \in (0, 1]$, while satisfying the achievability as implied by the observation (ii).

V. Solar Sail Trajectory Design with Mission Margins

A. Minimum Cone Angle Objectives

As discussed in Section IV, it is expected that attitude profiles with moderate cone angle values provide transfer trajectories with some margins in the direction along with the x-axis of the O-frame. Based on the observation, this study proposes a new set of objective metrics for solar sail trajectories, which minimize the cumulative cone angle over a transfer; this may be analogous to minimizing the fuel and energy (squared fuel) of conventional low-thrust trajectories.

It is noteworthy here that only the minimum ToF objective has been considered for solar-sail trajectory optimization in literature [8, 9, 26, 27]. While there is no need to consider other metrics than ToF if the planned transfers can be perfectly executed with no errors, such a perfect execution assumption is far from the reality in actual implementation of missions. The aim here is to improve the robustness of reference trajectories by designing them through the use of new objective metrics that enable moderate cone angle profiles. In fact, Mystic [28] has also implemented in its latest version the capability to optimize a similar quantity to the quadratic cone angle. In addition, having different control profiles than those with the minimum ToF objective implies that it is necessary to extend the nominal ToF when designing trajectories with such objectives, which provides mission designers with an additional degree of freedom.

Specifically, the following Lagrangian costs, $\mathcal{L}(\alpha)$, are considered in this study:

$$\mathcal{L} = \begin{cases} 1 & \text{Minimum time-of-flight} \\ \sin \alpha & \text{Minimum (linear) cone angle} \\ \sin^2 \alpha & \text{Minimum quadratic cone angle} \\ \sin^3 \alpha & \text{Minimum cubic cone angle} \end{cases} \tag{11}$$

6

and the solar-sail optimal transfer problems are formulated as follows:

$$\min_{\boldsymbol{x},\boldsymbol{u}\in\mathcal{U},t_0,t_f} \int_{t_0}^{t_f} k\mathcal{L}(\alpha)\mathrm{d}t$$

$$\text{s.t.} \quad \dot{\boldsymbol{x}} = \boldsymbol{f}_0(\boldsymbol{x},t) + F(\boldsymbol{x})\boldsymbol{a}_s(\boldsymbol{x},\boldsymbol{u}), \quad \boldsymbol{\psi}_0(\boldsymbol{x}_0,t_0) = 0, \quad \boldsymbol{\psi}_f(\boldsymbol{x}_f,t_f) = 0, \tag{12}$$

where $k > 0 \in \mathbb{R}$ is a scaling parameter and not optimized. Note that the first dynamics constraint corresponds to the equations of motion defined in Section II.B while the latter two represent the departure and arrival constraints.

B. Optimality Necessary Conditions

The optimality necessary conditions for the solar-sail optimal transfer problems Eq. (12) are derived by applying the calculus of variations and Pontryagin's optimality principle. The results presented in this paper extend the *solar sailing primer vector theory* developed in Ref. 12, which is focused on the minimum ToF solar-sail transfer problem. The main difference between the minimum-ToF solution and others lies in the optimal control law derived from Pontryagin's optimality principle, and therefore the derivation process here is focused on the difference.

For any of $\mathcal{L}(\alpha)$ in Eq. (11), the control Hamiltonian $\mathcal{H}$ can be expressed as:

$$\mathcal{H} = k\mathcal{L}(\alpha) + \boldsymbol{\lambda}^\top(\boldsymbol{f}_0(\boldsymbol{x},t) + F(\boldsymbol{x})\boldsymbol{a}_s(\boldsymbol{x},\boldsymbol{u})) = k\mathcal{L}(\alpha) + \boldsymbol{\lambda}^\top\boldsymbol{f}_0(\boldsymbol{x},t) - \boldsymbol{p}^\top\boldsymbol{a}_s(\boldsymbol{x},\boldsymbol{u}) \tag{13}$$

where $\boldsymbol{p} \triangleq -F\boldsymbol{\lambda}$ is termed *solar sailing primer vector* in Ref. 12 for its significance and properties analogous to Lawden's primer vector. Using Eq. (3), the control Hamiltonian can be also written as:

$$\mathcal{H} = k\mathcal{L}(\alpha) + \boldsymbol{\lambda}^\top\boldsymbol{f}_0(\boldsymbol{x},t) - \frac{\sigma G_0}{d^2}\cos\alpha \ \boldsymbol{p}^\top \begin{bmatrix} C_1\cos^2\alpha + C_2\cos\alpha + C_3 \\ -(C_1\cos\alpha + C_2)\sin\alpha\sin\beta \\ -(C_1\cos\alpha + C_2)\sin\alpha\cos\beta \end{bmatrix} \tag{14}$$

Applying the calculus of variations and Pontryagin's optimality principle yields the Euler-Lagrange equations and transversality conditions as necessary conditions of optimality. The optimal control law is obtained by solving

$$\boldsymbol{u}^* = \underset{\boldsymbol{u}\in\mathcal{U}}{\arg\min}\ \mathcal{H}(\boldsymbol{x},\boldsymbol{u},\boldsymbol{\lambda},t) = \underset{\boldsymbol{u}\in\mathcal{U}}{\arg\min}\ \left[\boldsymbol{\lambda}^\top\boldsymbol{f}_0(\boldsymbol{x},t) + \frac{\sigma G_0}{d^2}\bar{\mathcal{H}}(\boldsymbol{x},\boldsymbol{u},\boldsymbol{\lambda},t)\right] = \underset{\boldsymbol{u}\in\mathcal{U}}{\arg\min}\ \bar{\mathcal{H}}(\boldsymbol{x},\boldsymbol{u},\boldsymbol{\lambda},t), \tag{15}$$

where $\bar{\mathcal{H}}$ is introduced for compact notation and defined as:

$$\bar{\mathcal{H}} = \gamma\mathcal{L}(\alpha) - \cos\alpha \ \boldsymbol{p}^\top \begin{bmatrix} C_1\cos^2\alpha + C_2\cos\alpha + C_3 \\ -(C_1\cos\alpha + C_2)\sin\alpha\sin\beta \\ -(C_1\cos\alpha + C_2)\sin\alpha\cos\beta \end{bmatrix}, \quad \gamma \triangleq \frac{kd^2}{\sigma G_0}(>0). \tag{16}$$

C. Optimal Control Laws

Although $\boldsymbol{u}^*$ in Eq. (15) generally takes different forms depending on the choice of Lagrangian listed in Eq. (11), it is clear that β^* (β that minimizes $\mathcal{H}$) takes the same form regardless of the choice because any of $\mathcal{L}$ in Eq. (11) is not a function of β. Such β^* is derived in Ref. 12 as:

$$\beta^* = \arctan 2(-p_y, -p_z), \tag{17}$$

where $\arctan 2(Y, X)$ is the four-quadrant inverse tangent of Y and X. This is equivalently expressed as:

$$\sin\beta^* = -p_y/p_{yz}, \quad \cos\beta^* = -p_z/p_{yz}, \quad p_{yz} \triangleq \sqrt{p_y^2 + p_z^2}. \tag{18}$$

Unlike β^*, α^* takes different forms depending on the choice of Lagrangian listed in Eq. (11), which are obtained by solving the nonlinear optimization problem $\alpha^* = \arg\min \bar{\mathcal{H}}(\alpha, \beta = \beta^*)$ under the constraint $\alpha \in [\alpha_{\min}, \alpha_{\max}]$. Since the minimum of a general nonlinear function is given either at one of its local minima or at one of the boundaries of its domain, letting $\alpha_i^\star$ denote the i-th local minimum of $\bar{\mathcal{H}}$, α^* can be expressed as:

$$\alpha^* = \underset{\alpha\in\{\alpha_i^\star, \alpha_{\min}, \alpha_{\max}\}}{\arg\min}\ \bar{\mathcal{H}}(\alpha, \beta = \beta^*). \tag{19}$$

7

The local minima, $\alpha_i^\star$, are derived by applying the Legendre–Clebsch condition [29] to the control Hamiltonian as

$$\alpha_i^\star \in \arg_{\alpha \in [\alpha_{\min}, \alpha_{\max}]} \left[\bar{\mathcal{H}}_\alpha = 0 \ \wedge \ \bar{\mathcal{H}}_{\alpha\alpha} \geq 0 \right]_{\beta=\beta^*}, \tag{20}$$

where $\mathcal{H}_\alpha = \partial\mathcal{H}/\partial\alpha$ and $\mathcal{H}_{\alpha\alpha} = \partial^2\mathcal{H}/\partial\alpha^2$. To obtain $\alpha_i^\star$ that satisfy Eq. (20) for each Lagrangian in Eq. (11), this study takes the same approximation approach as used in Ref. 12; the approach first solves for $\alpha^\star$ that satisfy Eq. (20) for the ideal reflection model (i.e., $C_1 = 2$ and $C_2 = C_3 = 0$), denoted by $\alpha_0^\star$, and then approximates $\alpha^\star$ by the first-order Taylor expansion about $\alpha_0^\star$. Based on this approach, $\alpha^\star$ can be computed as:

$$\alpha^\star = \alpha_0^\star - \bar{\mathcal{H}}_\alpha(\alpha_0^\star)/\bar{\mathcal{H}}_{\alpha\alpha}(\alpha_0^\star). \tag{21}$$

The sub-optimality due to this approximation is confirmed to be virtually negligible for the minimum-ToF objective (i.e., $\mathcal{L} = 1$) through a comprehensive numerical study in Ref. 30.

The final step is to obtain analytical expression of $\alpha_0^\star$ for each $\mathcal{L}$ in Eq. (11). $\alpha_0^\star$ for the minimum-ToF objective (i.e., $\mathcal{L} = 1$) is derived in Ref. 12. $\alpha_0^\star$ for other $\mathcal{L}$ are first derived in this study; due to the page limitation, this paper presents only the solution to the quadratic one with a sketch of the derivation.

Minimum quadratic cone angle objective   As discussed above, $\alpha_0^\star$ is first analytically derived by solving Eq. (20) with the ideal reflection model and then used to approximate $\alpha^\star$. With $\mathcal{L} = \sin^2 \alpha$, the first-order condition of Eq. (20) is calculated (with some algebraic manipulations) as:

$$\bar{\mathcal{H}}_\alpha(\alpha, \beta = \beta^*) = \cos\alpha(6p_x \sin\alpha\cos\alpha - 3p_{yz}(1 - 2\sin^2\alpha) + p_{yz} + 2\gamma\sin\alpha) = 0. \tag{22}$$

A possible solution to Eq. (22), $\alpha = \pi/2$, can be eliminated from our consideration by using the second-order condition, implying that $\cos\alpha > 0$. Then, dividing $\bar{\mathcal{H}}_\alpha(\alpha, \beta = \beta^*)$ by $\cos\alpha$, introducing a variable transformation, $z \triangleq \sin\alpha$ (so $\cos\alpha = \sqrt{1 - z^2}$ since $\cos\alpha > 0$), and appropriately squaring the equation yields a fourth-order polynomial equation as:

$$\begin{aligned} &c_4 z^4 + c_3 z^3 + c_2 z^2 + c_1 z + c_0 = 0, \\ &c_4 = 9\,\|\boldsymbol{p}\|_2^2, \quad c_3 = 6p_{yz}\gamma, \quad c_2 = \gamma^2 - 6p_{yz}^2 - 9p_x^2, \quad c_1 = -2p_{yz}\gamma, \quad c_0 = p_{yz}^2 \end{aligned} \tag{23}$$

It is known that general quartic equations are analytically solvable (for instance via the Ferrari's method), although the solution expression is lengthy to explicitly write out. Computationally, such solutions can be easily obtained by using a polynomial root-finding functions, such as `roots(·)` in Matlab, `numpy.roots(·)` in Python, and `Polynomial(·)` with the `Polynomials.jl` package in Julia.

Once the roots of Eq. (23), denoted by $\{z_1, z_2, z_3, z_4\}$, are found, we can calculate candidate solutions for $\alpha_0^\star$ via $\arcsin z_i, i = 1, 2, 3, 4$ and select real solutions that satisfy the Legendre–Clebsch condition Eq. (20). Although this procedure itself may not seem reliable nor suited for the use in numerical optimization routines at a higher layer (i.e., trajectory optimization), it can be mathematically shown that $\bar{\mathcal{H}}_\alpha(\alpha, \beta = \beta^*)$ in Eq. (22) has a unique local minimum in $[0, \pi/2)$, implying that this procedure always gives the unique feasible $\alpha_0^\star$ in $[0, \pi/2)$, and thus eliminating the possibility of causing numerical instability and chattering of the solution. It also implies that, if $\alpha_0^\star$ is not contained in $[\alpha_{\min}, \alpha_{\max}]$, simply truncating the value at the boundary gives the minimum of $\bar{\mathcal{H}}_\alpha$, and therefore we can compute α^* as: $\alpha^* = \text{Median}(\alpha_{\min}, \alpha^\star, \alpha_{\max})$.

D. Reference Trajectory Examples with Mission Margins

Fig. 4 includes examples of solar sail trajectories designed with the minimum ToF objective and minimum quadratic cone angle objective via indirect methods (see Ref. 12 for details of the solution method). These trajectories are designed with $\alpha_{\max} = 47$ deg, which has 3 degrees of margins in the maximum cone angle. The target state of 2020 GE is modeled as a Keplerian orbit defined in Section III. Figs. 4(a) to 4(c) include the trajectory projected onto the $x-y$ plane in the Sun-Earth rotating frame, its 3-D view, and its control profile, respectively. For the trajectory with the minimum quadratic cone angle objective, only the optimized control profile is shown in Fig. 4(d), as the trajectory is not largely different from Fig. 4(a) (apart from the phase where the spacecraft rendezvous with the asteroid). The trajectory is designed with fixed 400-day ToF; note that ToFs of trajectories with newly proposed objective metrics need to be fixed to guarantee the uniqueness of the solution. It is obvious from Fig. 4(d) that the trajectory designed with the minimum quadratic cone angle objective yields margins in terms of a moderate cone angle profile, largely different from the one designed with the conventional minimum-ToF objective (Fig. 4(c)).
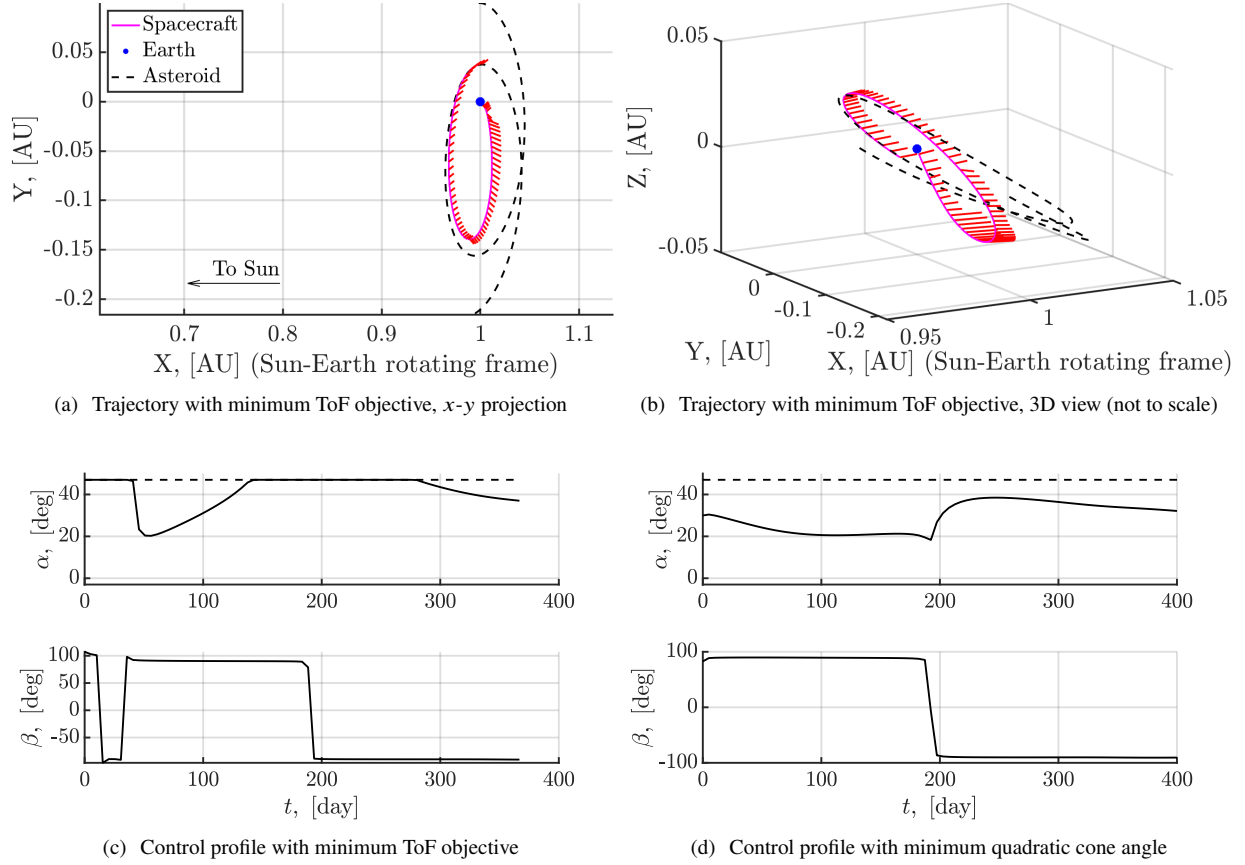
8

(a) Trajectory with minimum ToF objective, x-y projection

(b) Trajectory with minimum ToF objective, 3D view (not to scale)

(c) Control profile with minimum ToF objective

(d) Control profile with minimum quadratic cone angle

Figure 4   Optimal solar sailing trajectories with different objective metrics (see Section V.A) with $\alpha_{\max}$ = 47 deg. ToFs are ~367 days for the minimum-ToF trajectory and 400 days for the others.

As discussed in Section IV, this moderate cone angle profile contributes to keeping reference trajectories closer to the center of the reachable set. This is indeed confirmed by plotting the location of the nominal state with respect to the reachable set; the nominal state shown in Figs. 3(a) and 3(b) is in fact a result propagated with a moderate-cone angle profile in Fig. 4(d).

The other margin quantity, reduced y−z acceleration, is also implemented, where the optimal control laws remain the same by using ${}^O\boldsymbol{a}_s = [a_x \ \Gamma a_y \ \Gamma a_z]^\top$ in place of the original acceleration. As a result, it is confirmed that reference trajectories designed with $\Gamma < 1$ indeed contributes to pushing the nominal state inside the reachable set; specifically, trajectories designed with $\Gamma = 0.95$ and $\Gamma = 0.90$ for the same objective metric as in Fig. 4(d) are found inside the reachable set by the amount ~2×10^4 km and ~4×10^4 km at $t = t_f - 63$ [day], respectively. More thorough investigations are necessary to quantify how much robustness these margins would introduce to the reference trajectories.

E. Resilience against Safe-mode Events

The robustness gained by incorporating these margin quantities is quantified by evaluating and comparing the safe-mode resilience of trajectories designed with and without the candidate margins.

The *safe mode* is an operation mode of space missions triggered by a system-level fault detection, where spacecraft turn off onboard instruments that are not essential for maintaining their minimal functions and orient their attitude for power generation, thermal stability, and Earth communication. Safe mode events are not uncommon in space missions; almost 80% of one-year missions would experience at least one safe mode events based on statistical analysis [31].

In the context of low-thrust missions, a safe mode event occurring during a thrusting arc causes the spacecraft to miss the thrust ("missed thrust"). This leads to the spacecraft orbit drifting from the nominal trajectory, which then requires mission designers to redesign the transfer trajectory and update the orbit control commands. Ideally, reference

9

(a) Reference trajectory: minimum ToF

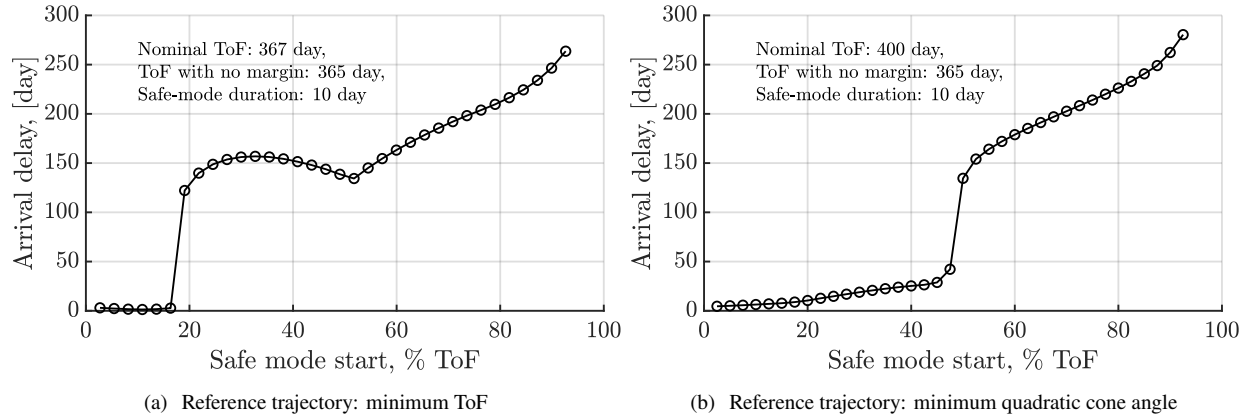(b) Reference trajectory: minimum quadratic cone angle

Figure 5   Safe mode analysis results. Recovery trajectories are designed after 10-day safe mode events with the minimum-ToF objective and a relaxed cone angle constraint $\alpha_{\max} = 48$ deg.

trajectories of low-thrust missions are designed to be resilient against such safe mode events, in the sense that they can recover from the deviations and achieve the mission objectives, for probable number and duration of safe mode events. For the significance of this problem in low-thrust missions, an increasing number of studies have investigated different approaches to address this problem, such as those based on the calculus of variations and stochastic approximation [32], on a direct method and virtual swarm optimization [33], and on expected thrust fraction [34]. There are also some studies focused on investigating the trade-off relations between the system margins [23] and estimating the margins that indicate the tolerance of low-thrust missions against safe mode events [35].

The influence of safe mode events is equally, perhaps much more, significant in solar sailing missions. When solar sail spacecraft enters a safe mode, the sail will keep generating acceleration in a direction that is not planned in the nominal trajectory. The direction of SRP acceleration during safe modes depends on the specific attitude the spacecraft is supposed to take for safing. The NEA Scout mission will orient the sail normal toward the Sun (i.e., $\alpha = 0$; zero cone angle), generating the maximum acceleration in the radial direction, which introduces greater perturbations than simply missing the thrust. Furthermore, the solution space for the redesign of recovery trajectories after safing is much smaller than that of low-thrust missions due to the less orbit controllability of solar sailing by nature.

The resilience of the reference trajectories designed with the candidate margins are evaluated by performing safe-mode analysis. In the analysis, safe-mode events (assumed to last 10 days) are simulated on a trajectory in a deterministic manner, and recovery trajectories are optimized after the end of each safing. The analysis procedure is similar to the one presented in Ref. 35, whereas in this study the recovery trajectory optimization process uses the indirect method developed in Ref. 12 and takes into account the non-ideal sail model and attitude constraint, which are found to have huge influence on the trajectory feasibility and arrival lateness.

A portion of the results obtained in this analysis are presented in Fig. 5, where those in Fig. 4 are taken as the reference trajectories. The figures show the arrival delays of recovery trajectories, where each recovery trajectory is designed with the minimum-ToF objective to assess the minimum arrival delays. The arrival delays are measured with respect to ~365 days, the ToF of a trajectory designed with no margin (i.e., minimum-ToF objective, $\alpha_{\max} = 50$ deg). Comparing Figs. 5(a) and 5(b), the latter shows much less arrival delays when a safe mode happens during the first half of the transfer, while the last half does not seem to have a large difference. In particular, arrival delays of more than 100 days are not desirable as it entails a greater Earth-spacecraft distance at the time of asteroid rendezvous than allowed for the data downlink phase to complete within a planned period. This implies that it would be crucial to continue exploring other approaches to enhancing the resilience against safe mode events, including incorporating other margin quantities that satisfy the requirements discussed in Section IV.A.

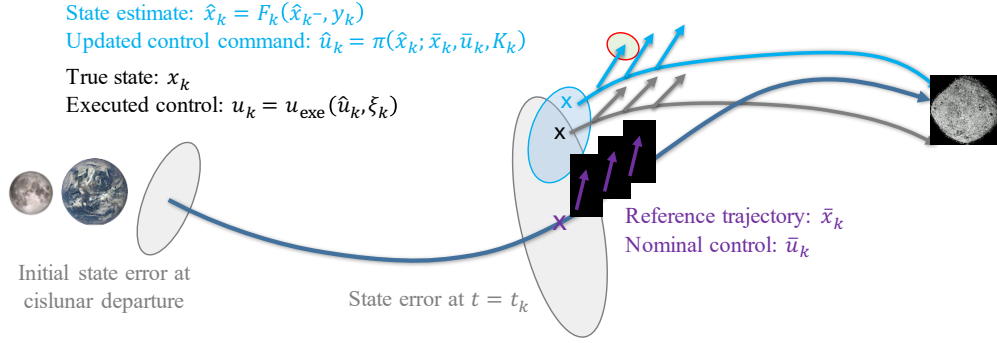## VI. Robust Trajectory Design under Navigation & Control Errors

Figure 6   Notional operation sequence of low-thrust trajectory corrections under navigation and control errors

A. Trajectory Design under Uncertain Errors

As discussed in Section I, any space trajectories are subject to uncertain errors, such as navigation and control errors. Particularly, in low-thrust missions, mission designers need to regularly redesign the trajectories in response to those errors to update the control commands transmitted to spacecraft. A notional operation sequence of low-thrust trajectory corrections under uncertainty is schematically depicted in Fig. 6; this operation sequence can be described as follows: first, the spacecraft orbital state is controlled by applying a nominal control history; however, due to errors in the initial state and control executions, the actual state will drift from the reference trajectory with growing state uncertainty (gray ellipse); mission designers will become aware of this deviation as a result of orbit determination (OD) with navigation uncertainty (blue ellipse) and redesign the reference based on the state estimate (blue cross), which will shrink the state error; the updated control commands are executed on orbit with a control error (red ellipse), increasing the state error and requiring future trajectory corrections that repeat the same procedure as just described.

Our goal as mission designers is to ensure that the mission will successfully achieve its objective (e.g., rendezvous with the target asteroid) as a result of the repeated redesign of trajectories under navigation and control errors following the procedure described above.

The same discussion equally applies to solar sailing trajectories. Even worse, solar sailing missions are expected to have a greater amount of uncertainty both in the navigation and control errors; the difficulty in perfectly modeling the force caused by SRP may decrease the accuracy of OD solutions and is expected to introduce greater uncertainty in the control error, which jointly lead to greater uncertain state errors. The complex attitude behavior of the sail made of thin, flexible films would further degrade the control execution accuracy. Our objective as the NEA Scout mission design team is to design reference trajectories with guaranteed successful rendezvous while dealing with these severe uncertain state errors.

To address this problem, our stochastic approach develops a reference trajectory design method based on stochastic optimal control. The approach developed in this study combines techniques recently developed in the fields of control and optimization, including linear covariance steering with output feedback [36] and successive convexification for nonlinear trajectory optimization [37–39].

B. Problem Statement

1. Nonlinear Stochastic System

When we incorporate uncertain errors in our mission design process, one of the most straightforward approaches would be to express our system via nonlinear stochastic differential equations (SDEs). Based on the equations of motion presented in Section II.B, our stochastic system can be formally expressed as:

$$d\boldsymbol{x} = \boldsymbol{f}(\boldsymbol{x}, \boldsymbol{u}, t)dt + g(\boldsymbol{x}, \boldsymbol{u})d\boldsymbol{w}(t), \tag{24}$$

where $g(\cdot)$ represents the intensity of control execution errors; recall from Section II.B that $\boldsymbol{f}(\cdot)$ represents the orbital dynamics under control. $d\boldsymbol{w}(t) \in \mathbb{R}^{n_w}$ is standard Brownian motion, i.e., $\mathbb{E}[d\boldsymbol{w}] = 0$ and $\mathbb{E}[d\boldsymbol{w}(t)d\boldsymbol{w}^\top(t)] = I dt$. The nominal (or reference) trajectories of the state and control are denoted by $\boldsymbol{x}^{\text{ref}}$ and $\boldsymbol{u}^{\text{ref}}$, respectively.

We assume that the state information is partially available through a discrete-time observation process as:

$$y_k = f_o(x_k) + g_o(x_k)v_k, \tag{25}$$

where $y_k \in \mathbb{R}^{n_y}$ is the measurement, and $v_k \in \mathbb{R}^{n_y}$ is measurement noise, with $\mathbb{E}[v_k] = 0$ and $\mathbb{E}\left[v_i v_j^\top\right] = \delta_{i,j}I$; $\delta_{i,j}$ is the Kronecker delta. $k(= 0, 1, ..., N)$ denotes the discrete time steps where observations y_k are available. Based on observations $y_i(i = 0, 1, ..., k)$, the current state estimate, $\hat{x}_k$, is obtained by a filtering process as follows:

$$\hat{x}_k = \mathcal{F}_k(\hat{x}_0^-, y_i : i = 0, 1, ..., k), \tag{26}$$

where the "−" super script indicates a quantity right before the measurement update. The initial state distribution, x_0, and its estimate, $\hat{x}_0^-$, are assumed to be known (or can be estimated, perhaps conservatively). The estimation error is denoted by $\tilde{x}_k = x_k - \hat{x}_k$.

The trajectory redesign process discussed in Section VI.A is modeled by a sequence of feedback policies that compute trajectory corrections based on a history of state estimates. The feedback policies are thus expressed as:

$$u_k = \pi_k(x_k^{\text{ref}}, u_k^{\text{ref}}, \Omega_k, \hat{x}_i : i = 0, 1, ..., k-1), \tag{27}$$

where Ω_k denotes a set of parameters used to compute the corrective control input u_k according to the policy π_k.

2. Original Problem

As discussed in Ref. 14, an expectation-based formulation allows a greater flexibility in formulating various types of cost and constraint functions, encompassing those involving expected values, covariance matrices, and higher-order moments. The expectation-based formulation with an auxiliary function $\phi(\cdot)$ is given by [14]

$$J = \mathbb{E}[\phi(Z)] = \int \phi(z)f_{\text{pdf}}(z)\mathrm{d}z, \tag{28}$$

where the integral is computed over the support of Z; $f_{\text{pdf}}(\cdot)$ denotes the associated probability density function.

While the flexibility provided by the expectation-based formulation is helpful when considering a broader variety of problems, this study departs from this abstract expression and considers a focused form of cost and constraint functions in the following. Nevertheless, the basic idea behind the discussion below will remain valid with the expectation-based formulation, although an approach to constructing a convex subproblem may be different depending on the specific forms of $\phi(Z)$ in Eq. (28).

Specifically, the cost function considered in this study is expressed as summation of stage costs:

$$J = \sum_{k=0}^{N} \mathcal{L}_k(x_k, u_k, t_k) \tag{29}$$

The constraints considered in this study include path chance constraints and state terminal constraints. The path chance constraints are imposed on discrete-time state and control at time t_k as:

$$\mathbb{P}\left[c_{x_j}(x_k, t_k) \le 0\right] \ge 1 - \varepsilon_{x_j}, \quad \mathbb{P}\left[c_{u_j}(u_k, t_k) \le 0\right] \ge 1 - \varepsilon_{u_j}, \quad \forall j, \tag{30}$$

where $\mathbb{P}[\cdot]$ denotes the probability operator, $c_{x_j}(\cdot)$ and $c_{u_j}(\cdot)$ represent the j-th nonlinear constraint function, and ε_{x_j} and ε_{u_j} are risk bounds associated with the j-th constraints. This imposes the constraint $c_j \le 0$ to be satisfied with probability greater than or equal to $1 - \varepsilon_j$; see, for instance, Ref. 16 and references therein, for the use of chance constraints in the context of space trajectory optimization. The terminal constraint is imposed to make sure that the designed trajectory nominally achieves the target x_f with prescribed accuracy represented by the final covariance P_f:

$$x_N^{\text{ref}} - x_f = 0, \quad P_N \preceq P_f \tag{31}$$

where P_N denotes the covariance of the final state under the action of corrective controls Eq. (27).

Thus, our original problem can be expressed as in Problem 1.

Problem 1 (Original problem). *Find $x^{\text{ref}}(t), u_k^{\text{ref}}, \pi_k,$ and Ω_k that minimize the cost Eq. (29) while satisfying the dynamical constraint Eq. (24), chance constraints Eq. (30), and terminal constraint Eq. (31) under a sequence of corrective control updates determined by Eq. (27) with the state estimates Eq. (26) based on observations Eq. (25).*

12

C. Sequential Convex Programming Approach

Problem 1 does not generally have closed-form solutions. Furthermore, its numerical solution is typically expensive, if not intractable, to solve exactly. In particular, the process of *uncertainty quantification* (UQ) involving nonlinear dynamics, cost, and constraints is a major bottleneck of the numerical solution process, as it typically requires performing expensive UQ processes many times to evaluate the functions and their gradients. Among multiple possible approaches, a solution method based on sequential convex programming is developed to solve our problem in this study. The solution method combines techniques recently developed in the fields of control and optimization, including linear covariance steering with output feedback [36] and successive convexification for nonlinear trajectory optimization [37–39].

The proposed approach approximately formulates the originally expensive problem, including the UQ process, in a convex form at each successive iteration. At each iteration, the original problem is approximated as a convex subproblem, which is solved with guaranteed convergence due to the convex property, and then the solution to a convex subproblem is used as a new reference trajectory for the next iteration. Leveraging the reliability and efficiency of convex programming, this solution method enables us to overcome the major bottleneck of numerical solutions to stochastic optimal control problems, in exchange for approximate dynamical evolution of the stochastic states about the reference trajectory. Note that the dynamical feasibility of the reference trajectory is guaranteed in our solution method, as discussed in Section VI.C.3.

This approach assumes that the initial state and initial state estimate are Gaussian-distributed about the reference, i.e., $\boldsymbol{x}_0 \sim \mathcal{N}(\boldsymbol{x}_0^{\text{ref}}, P_0)$ and $\hat{\boldsymbol{x}}_0 \sim \mathcal{N}(\boldsymbol{x}_0^{\text{ref}}, \hat{P}_0^-)$, although this assumption may be removed by extending the approach, for instance, by using a mixture of Gaussian distributions to model the initial distribution. The convex subproblem that approximates Problem 1 is formulated based on Ref. 36, which is briefly reviewed below with some modifications.

1. Linear Block-Matrix Formulation with Output Feedback

To obtain the convex subproblem, Eq. (24) is first linearized and discretized assuming fixed-time problems (i.e., t_0 and t_f not part of optimization variables); extending the following discussion to time-varying problems is straightforward by incorporating the time normalization variable s (defined immediately below) as part of control variables.

Defining s as $s \triangleq \frac{\mathrm{d}t}{\mathrm{d}\tau}$, the time can be normalized by s with $\tau \in [0, 1]$, yielding:

$$\mathrm{d}\boldsymbol{x} = s\boldsymbol{f}(\boldsymbol{x}, \boldsymbol{u}, \tau)\mathrm{d}\tau + \sqrt{s}g(\boldsymbol{x}, \boldsymbol{u})\mathrm{d}\boldsymbol{w}(\tau). \tag{32}$$

Then the linearized dynamics about the reference trajectory $\boldsymbol{x}^{\text{ref}}(\tau)$ and $\boldsymbol{u}^{\text{ref}}(\tau)$ are

$$\mathrm{d}\boldsymbol{x} \approx \left[s^{\text{ref}} \frac{\partial \boldsymbol{f}^{\text{ref}}}{\partial \boldsymbol{x}} (\boldsymbol{x} - \boldsymbol{x}^{\text{ref}}) + s^{\text{ref}} \frac{\partial \boldsymbol{f}^{\text{ref}}}{\partial \boldsymbol{u}} (\boldsymbol{u} - \boldsymbol{u}^{\text{ref}}) + s\boldsymbol{f}^{\text{ref}}(\tau) \right] \mathrm{d}\tau + \sqrt{s^{\text{ref}}}g^{\text{ref}}(\tau)\mathrm{d}\boldsymbol{w}(\tau), \tag{33}$$

where the "ref" superscript on a quantity (function) indicates that the quantity (function) is evaluated on the reference trajectory, i.e., $\boldsymbol{f}^{\text{ref}}(\tau) \triangleq \boldsymbol{f}(\boldsymbol{x}^{\text{ref}}(\tau), \boldsymbol{u}^{\text{ref}}(\tau), \tau)$ and $g^{\text{ref}}(\tau) \triangleq g(\boldsymbol{x}^{\text{ref}}(\tau), \boldsymbol{u}^{\text{ref}}(\tau), \tau)$. The linearized dynamics can be equivalently expressed as:

$$\mathrm{d}\boldsymbol{x} \approx [A(\tau)\boldsymbol{x} + B(\tau)\boldsymbol{u} + \boldsymbol{h}(\tau)]\mathrm{d}\tau + G(\tau)\mathrm{d}\boldsymbol{w}(\tau), \tag{34}$$

where

$$A = s^{\text{ref}} \frac{\partial \boldsymbol{f}^{\text{ref}}}{\partial \boldsymbol{x}}, \quad B = s^{\text{ref}} \frac{\partial \boldsymbol{f}^{\text{ref}}}{\partial \boldsymbol{u}}, \quad \boldsymbol{h} = s^{\text{ref}}\boldsymbol{f}^{\text{ref}} - A\boldsymbol{x}^{\text{ref}} - B\boldsymbol{u}^{\text{ref}}, \quad G = \sqrt{s^{\text{ref}}}g^{\text{ref}}. \tag{35}$$

Integrating Eq. (34) over each interval $[t_k, t_{k+1})$ with zero-order-hold control (i.e., $\boldsymbol{u}(t) = \boldsymbol{u}_k, \forall t \in [t_k, t_{k+1})$) yields

$$\boldsymbol{x}_{k+1} = A_k\boldsymbol{x}_k + B_k\boldsymbol{u}_k + \boldsymbol{h}_k + G_k\boldsymbol{w}_k, \tag{36}$$

where $\boldsymbol{w}_k$ is a standard n_w-dimensional Gaussian random vector and the matrices are defined as:

$$A_k = \Phi(\tau_{k+1}, \tau_k), \quad B_k = A_k \int_{\tau_k}^{\tau_{k+1}} \Phi^{-1}(\tau, \tau_k)B(\tau)\mathrm{d}\tau, \quad \boldsymbol{h}_k = A_k \int_{\tau_k}^{\tau_{k+1}} \Phi^{-1}(\tau, \tau_k)\boldsymbol{h}(\tau)\mathrm{d}\tau \tag{37}$$

and G_k is any matrix such that $G_k\boldsymbol{w}_k$ has covariance

$$A_k \left\{ \int_{\tau_k}^{\tau_{k+1}} \Phi^{-1}(\tau, \tau_k)G(\tau)[\Phi^{-1}(\tau, \tau_k)G(\tau)]^\top \mathrm{d}\tau \right\} A_k^\top \tag{38}$$

13

$\Phi(\tau_j, \tau_i)$ denotes a state transition matrix (STM) from τ_i to τ_j and can be computed as:

$$\frac{d}{d\tau}\Phi(\tau, \tau_k) = A(\tau)\Phi(\tau, \tau_k), \quad \Phi(\tau_k, \tau_k) = I \tag{39}$$

For convex formulation, the trajectory correction policies are modeled as a sequence of affine filtered state history feedback controllers. That is, $\boldsymbol{u}_k$ is calculated as an affine function of previous state estimates $\hat{\boldsymbol{x}}_0, \hat{\boldsymbol{x}}_1, ..., \hat{\boldsymbol{x}}_k$:

$$\boldsymbol{u}_k = \boldsymbol{u}_k^{\text{ref}} + \sum_{i=0}^{k} K_{k,i}(\hat{\boldsymbol{x}}_i - \boldsymbol{x}_i^{\text{ref}}), \tag{40}$$

where $K_{k,i}$ are feedback gain matrices to be optimized. Since the state is initially Gaussian-distributed and obeys the linear dynamics in a convex subproblem, the optimal state estimate can be obtained by the Kalman filter, enabling us to model the filtration process Eq. (26) in a linear form as:

$$
\begin{aligned}
\hat{\boldsymbol{x}}_k^- &= A_{k-1}\hat{\boldsymbol{x}}_{k-1} + B_{k-1}\boldsymbol{u}_{k-1} + \boldsymbol{h}_{k-1}, & \tilde{P}_k^- &= A_{k-1}\tilde{P}_{k-1}^- A_{k-1}^\top + G_{k-1}G_{k-1}^\top, & \text{(time update)} \\
\hat{\boldsymbol{x}}_k &= \hat{\boldsymbol{x}}_k^- + L_k(\boldsymbol{y}_k - C_k\hat{\boldsymbol{x}}_k^-), & \tilde{P}_k &= (I - L_kC_k)\tilde{P}_k^-(I - L_kC_k)^\top + L_kD_kD_k^\top L_k^\top, & \text{(meas. update)}
\end{aligned} \tag{41}
$$

where $\tilde{P}_k$ denotes the estimate error covariance; L_k is the Kalman gain; C_k and D_k are of the linearized measurement equation about the reference. L_k, C_k, and D_k are given by

$$L_k = \tilde{P}_k^- C_k^\top (C_k\tilde{P}_k^- C_k^\top + D_kD_k^\top)^{-1}, \quad C_k = \frac{\partial \boldsymbol{f}_o^{\text{ref}}}{\partial \boldsymbol{x}}, \quad D_k = \frac{\partial \boldsymbol{g}_o^{\text{ref}}}{\partial \boldsymbol{x}}, \tag{42}$$

which implies that, as classically known in estimation theory, $\tilde{P}_k$ and L_k can be computed *a priori* for linear systems.

Combining Eqs. (36) and (41), the estimated state process under control can be directly written as:

$$\hat{\boldsymbol{x}}_{k+1} = A_k\hat{\boldsymbol{x}}_k + B_k\boldsymbol{u}_k + \boldsymbol{h}_k + L_{k+1}\tilde{\boldsymbol{y}}_{k+1}^-, \tag{43}$$

where $\tilde{\boldsymbol{y}}_k^-$ (also called *innovation process*) is defined as in Eq. (44). Eq. (44) also includes the expression for its covariance, denoted by $P_{\tilde{y}_k^-}$, whose derivation is straightforward by noting the independency between $\tilde{\boldsymbol{x}}_k, \boldsymbol{w}_i, \boldsymbol{v}_i, \forall i = 1, 2, ..., k-1$.

$$\tilde{\boldsymbol{y}}_k^- = \boldsymbol{y}_k - C_k\hat{\boldsymbol{x}}_k^-(= C_k\tilde{\boldsymbol{x}}_k + D_k\boldsymbol{v}_k), \quad P_{\tilde{y}_k^-} \triangleq \text{Cov}\left[\tilde{\boldsymbol{y}}_k^-\right] = C_k\tilde{P}_k^- C_k^\top + D_kD_k^\top. \tag{44}$$

The estimated state process Eq. (43) is equivalently written in a block-matrix form as:

$$
\begin{bmatrix} \hat{\boldsymbol{x}}_0 \\ \hat{\boldsymbol{x}}_1 \\ \hat{\boldsymbol{x}}_2 \\ \vdots \end{bmatrix} = \begin{bmatrix} I_{n_x} \\ A_0 \\ A_1A_0 \\ \vdots \end{bmatrix} \hat{\boldsymbol{x}}_0^- + \begin{bmatrix} 0_{n_x,n_u} & 0_{n_x,n_u} \\ B_0 & 0_{n_x,n_u} \\ A_1B_0 & B_1 \\ & & \ddots \end{bmatrix} \begin{bmatrix} \boldsymbol{u}_0 \\ \boldsymbol{u}_1 \\ \boldsymbol{u}_2 \\ \vdots \end{bmatrix} + \begin{bmatrix} 0_{n_x,n_x} & 0_{n_x,n_x} \\ I_{n_x} & 0_{n_x,n_x} \\ A_1 & I_{n_x} \\ & & \ddots \end{bmatrix} \begin{bmatrix} \boldsymbol{h}_0 \\ \boldsymbol{h}_1 \\ \boldsymbol{h}_2 \\ \vdots \end{bmatrix} + \begin{bmatrix} L_0 & 0_{n_x,n_y} \\ A_0L_0 & L_1 \\ A_1A_0L_0 & A_1L_1 \\ & & \ddots \end{bmatrix} \begin{bmatrix} \tilde{\boldsymbol{y}}_0^- \\ \tilde{\boldsymbol{y}}_1^- \\ \tilde{\boldsymbol{y}}_2^- \\ \vdots \end{bmatrix}
$$

which can be expressed in a compact form as:

$$X = \mathbf{A}\hat{\boldsymbol{x}}_0^- + \mathbf{B}U + H + \mathbf{L}\tilde{Y}, \tag{45}$$

where the matrix and vector quantities are defined accordingly.

2. Convex Subproblem

Now, with our equations of motion formulated in a block-matrix form in Eq. (45), we can analytically calculate the mean and covariance of $\{X, U\}$ under feedback controls in Eq. (40), as follows (see Theorem 3.1 of Ref. [36]):

$$\bar{X} \triangleq \mathbb{E}\left[\hat{X}\right] = \mathbf{A}\boldsymbol{x}_0^{\text{ref}} + \mathbf{B}\bar{U} + H, \quad \hat{P} \triangleq \text{Cov}\left[\hat{X}\right] = (I_{n_x} + \mathbf{BF})\mathbf{S}(I_{n_x} + \mathbf{BF})^\top, \quad P_U \triangleq \text{Cov}\left[U\right] = \mathbf{FSF}^\top, \tag{46}$$

where $\bar{U} \triangleq \mathbb{E}[U]$ is part of our feedback policies to be optimized (note that $\bar{\boldsymbol{u}}_k \triangleq \mathbb{E}[\boldsymbol{u}_k] = \boldsymbol{u}_k^{\text{ref}}$ in our linear system), and $\mathbf{F}$ and $\mathbf{S}$ are defined as:

$$\mathbf{F} = \mathbf{K}(I_{n_x} - \mathbf{BK})^{-1}, \quad \mathbf{S} = \mathbf{A}\hat{P}_0^- \mathbf{A}^\top + \mathbf{L}\mathbf{P}_{\tilde{Y}}\mathbf{L}^\top, \quad \mathbf{P}_{\tilde{Y}} = \text{blkdiag}(P_{\tilde{y}_0^-}, ..., P_{\tilde{y}_N^-}). \tag{47}$$

14

K consists of the feedback gain matrices $K_{k,i}$ and is defined as follows:

$$
\mathbf{K} = \begin{bmatrix}
K_{0,0} & 0_{n_u,n_x} & 0_{n_u,n_x} & \dots & 0_{n_u,n_x} \\
K_{1,0} & K_{1,1} & \ddots & \dots & 0_{n_u,n_x} \\
\vdots & \vdots & \ddots & 0_{n_u,n_x} & 0_{n_u,n_x} \\
K_{N-1,0} & K_{N-1,1} & \dots & K_{N-1,N-1} & 0_{n_u,n_x}
\end{bmatrix},
\tag{48}
$$

and can be computed from **F** as:

$$
\mathbf{K} = \mathbf{F}(I_{n_x} + \mathbf{BF})^{-1}
\tag{49}
$$

Based on these equations, the cost and constraints can be formulated in convex forms, likely with linearization or other convexification techniques, which largely depend on their functional forms. For instance, if the cost function depend only on the reference state and control, its convex counterpart is given by:

$$
J_{\text{cvx}} = J^{\text{ref}} + \sum_{k=0}^{N} \frac{\partial J^{\text{ref}}}{\partial \boldsymbol{x}_k} \delta \bar{\boldsymbol{x}}_k + \sum_{k=0}^{N-1} \frac{\partial J^{\text{ref}}}{\partial \boldsymbol{u}_k} \delta \bar{\boldsymbol{u}}_k,
\tag{50}
$$

where $\delta \bar{\boldsymbol{x}}_k$ ($\delta \bar{\boldsymbol{u}}_k$) denote the difference between the mean state (control) and the reference at step k. Note that $\delta \bar{\boldsymbol{x}}_k$ is affine in $\bar{X}$ since it can be expressed as: $\delta \bar{\boldsymbol{x}}_k = E_{x_k} \bar{X} - \boldsymbol{x}_k^{\text{ref}}$, where E_{x_k} is a matrix that extracts the k-th state from $\bar{X}$; likewise, $\delta \bar{\boldsymbol{u}}_k = E_{u_k} \bar{U} - \boldsymbol{u}_k^{\text{ref}}$. By assuming that the distribution of the output of $c_{x_j}(\cdot)$ can be approximately modeled as a Gaussian distribution, our state chance constraint in Eq. (30) can be expressed in a deterministic form as [16]:

$$
\texttt{norminv}(1 - \varepsilon_{x_j}) \left\| \frac{\partial c_{x_j}^{\text{ref}}}{\partial \boldsymbol{x}_k} P_k^{1/2} \right\|_2 + \frac{\partial c_{x_j}^{\text{ref}}}{\partial \boldsymbol{x}_k} \delta \bar{\boldsymbol{x}}_k + c_{x_j}^{\text{ref}} \leq 0,
\tag{51}
$$

where $P_k^{1/2}$ satisfies $P_k^{1/2}(P_k^{1/2})^\top = P_k$, and P_k is the state covariance at t_k. $\texttt{norminv}(\cdot)$ is the inverse function of the cumulative distribution function of the standard normal distribution, and $\texttt{norminv}(1 - \varepsilon_{x_j}) \geq 0$ assuming $\varepsilon_{x_j} \leq 0.5$, i.e., small risk bounds. Noting that $P_k = \hat{P}_k + \tilde{P}_k$, $P_k^{1/2}$ is equivalently expressed as:

$$
P_k^{1/2} = (E_{x_k} \hat{P} E_{x_k}^\top + \tilde{P}_k)^{1/2} = \begin{bmatrix} E_{x_k}(I_{n_x} + \mathbf{BF})\mathbf{S}^{1/2} & \tilde{P}_k^{1/2} \end{bmatrix}
\tag{52}
$$

which implies that Eq. (51) is convex in **F** and $\delta \bar{\boldsymbol{x}}_k$ (hence in $\bar{X}$). The control chance constraint can be also expressed in a convex form in the same manner. The terminal constraints are also reformulated in convex forms as [36]:

$$
E_{x_N} \bar{X} - \boldsymbol{x}_f = 0, \quad \left\| (P_f - \tilde{P}_N)^{-1/2} E_{x_N}(I_{n_x} + \mathbf{BF})\mathbf{S}^{1/2} \right\| - 1 \leq 0
\tag{53}
$$

Our convex subproblem is thus formulated as in Problem 2. Note that the covariance dynamics in Eq. (46) are not explicitly computed within the convex subproblem as $P_k^{1/2}$ is used for computing the cost and constraints.

Problem 2 (Convex subproblem). *Find* $\bar{X}, \bar{U}, \mathbf{F}$ *that minimize the convexified cost (e.g., Eq. (50)) subject to the mean and covariance dynamical constraint Eq. (46), chance constraints Eq. (51), and terminal constraint Eq. (53).*

3. Sequential Convex Programming with Penalty Method

Our solution method alternately constructs and solves the convex subproblem Problem 2 while updating the reference trajectory based on the subproblem result, marching toward the overall convergence. While each subproblem is guaranteed to converge due to the convexity, the reference updating process needs to have a mechanism to check the solution validity in the original nonlinear system, as each iteration relies on a linearized system. To address this, this study adopts an approach proposed in Ref. 38, which proves the convergence of their approach to a local optimum of the original problem and its convergence rate.

An important aspect of the approach is to avoid unfavorable situations that are known to occur in general successive convexification frameworks, if naïvely formulated. As detailed in Ref. 38, a naïve formulation may lead to *artificial*

unboundedness and *artificial infeasibility*. This study bases our solution method on their approach with some modifications to address these issues. Specifically, to mitigate artificial unboundedness, the trust region method is employed to bound the feasible regions of the variables $\bar{X}$ and $\bar{U}$ at each iteration; to avoid artificial infeasibility, the penalty method is utilized to allow some constraint violations and penalize the violations by augmenting the cost function in each subproblem. Note that the approach in Ref. 38 also uses *virtual control* to make each dynamical constraint feasible, which is deemed unnecessary in our block-matrix formulation.

The augmented cost and trust region constraints are described in Eqs. (54) and (55), respectively, where g_i^{ineq} ($i = 1, 2, ..., N_c$) are collection of inequality constraints. $v^{\text{eq}}, v_i^{\text{ineq}}$ are sufficiently large penalty weights and satisfy $v_i^{\text{ineq}} = 0$ when $g_i^{\text{ineq}} \leq 0$ while $v_i^{\text{ineq}} > 0$ when $g_i^{\text{ineq}} > 0$. Δ_x, Δ_u are the trust regions.

$$J_{\text{cvx,aug}} = J_{\text{cvx}} + v^{\text{eq}} \left\| E_{x_N} \bar{X} - \boldsymbol{x}_f \right\|_2^2 + \sum_{i=1}^{N_c} v_i^{\text{ineq}} (g_i^{\text{ineq}})^2, \tag{54}$$

$$\left\| E_{x_k} \bar{X} - \boldsymbol{x}_k^{\text{ref}} \right\|_\infty \leq \Delta_x, \quad \left\| E_{u_k} \bar{U} - \boldsymbol{u}_k^{\text{ref}} \right\|_\infty \leq \Delta_u. \tag{55}$$

Our modified convex subproblem is thus formulated as in Problem 3.

Problem 3 (Convex subproblem with trust regions and penalized cost). *Find $\bar{X}, \bar{U}, \mathbf{F}$ that minimize the penalized cost Eq. (54) subject to the mean and covariance dynamical constraint Eq. (46) and trust region constraint Eq. (55).*

At each iteration after a subproblem is solved, the penalty weights $v^{\text{eq}}, v_i^{\text{ineq}}$ are increased if the associated constraints are violated. Whether updating the reference or not depends on the the ratio of the actual cost change to the predicted change, denoted by ρ. If ρ is greater than a prescribed value, the reference $\{\boldsymbol{x}_k^{\text{ref}}, \boldsymbol{u}_k^{\text{ref}}\}$ is replaced by $\{\bar{X}, \bar{U}\}$; otherwise, the reference is not changed, and the same convex subproblem is solved with a smaller trust region. See Ref. 38 for more detail and its theoretical justification. A key difference in our formulation is the evaluation of the nonlinear cost; our formulation does not take into account the nonlinear cost and penalties that are dependent on stochastic terms, as precisely evaluating these quantities (i.e., nonlinear UQ) itself can be too computationally expensive to perform every iteration. Accordingly, only the deterministic components are incorporated in the computation of ρ.

D. Numerical Example: NEA Scout Robust Trajectory Optimization

The developed stochastic optimal control approach is applied to the design of interplanetary cruise trajectories of the NEA Scout mission. The dynamical model takes into account the third-body perturbation due to the Earth gravity as discussed in Section III. The state vector $\boldsymbol{x}$ is taken as the spacecraft position and velocity in Cartesian coordinates attached to a Sun-centered inertial frame (ECLIPJ2000); the control vector $\boldsymbol{u}$ consists of the attitude angle.

Major uncertain errors relevant to the current mission design process include the initial state dispersion, control execution errors, and orbit determination (OD) errors, all of which can be handled within the framework presented thus far in this section. The initial state dispersion is modeled as a Gaussian distribution of covariance $P_0 = \text{blkdiag}(\sigma_{r0}^2 I_3, \sigma_{v0}^2 I_3)$, where $\{\sigma_{r0}, \sigma_{v0}\}$ denote the standard deviations of the position and velocity dispersion at the epoch of cislunar escape. Their specific values are assumed to be $\{\sigma_{r0}, \sigma_{v0}\} = \{1,000 \text{ km}, 1.0 \text{ m/s}\}$.

The execution error is modeled to take into account the pointing and magnitude errors. The erroneous SRP acceleration vector $\tilde{\boldsymbol{a}}_s$ in the orbit frame is modeled as:

$$^O\tilde{\boldsymbol{a}}_s = \|\boldsymbol{a}_s\|_2 \, T(^O\boldsymbol{a}_s) \begin{bmatrix} \sin(\sigma_p w_p) \cos(2\pi w_\theta) \\ \sin(\sigma_p w_p) \sin(2\pi w_\theta) \\ \sigma_m w_m + \cos(\sigma_p w_p) - 1 \end{bmatrix} \tag{56}$$

where $\{\sigma_m, \sigma_p\}$ are the standard deviations of magnitude and pointing errors, $\{w_m, w_p\}$ are standard Gaussian random variables, w_θ is a standard uniform-distributed random variable, and $T(\cdot)$ is defined as:

$$T(\boldsymbol{a}_s) = \begin{bmatrix} \hat{\boldsymbol{S}} & \hat{\boldsymbol{E}} & \hat{\boldsymbol{Z}}, \end{bmatrix}, \quad \hat{\boldsymbol{Z}} = \frac{\boldsymbol{a}_s}{\|\boldsymbol{a}_s\|_2}, \quad \hat{\boldsymbol{E}} = \frac{[0, 0, 1]^\top \times \hat{\boldsymbol{Z}}}{\left\|[0, 0, 1]^\top \times \hat{\boldsymbol{Z}}\right\|_2}, \quad \hat{\boldsymbol{S}} = \hat{\boldsymbol{E}} \times \hat{\boldsymbol{Z}} \tag{57}$$

The specific values of $\{\sigma_m, \sigma_p\}$ are assumed to be $\{\sigma_m, \sigma_p\} = \{1.5 \%, 1.5 \text{ deg}\}$, which are based on the current estimate of the NEAS GNC team. As the expression in Eq. (56) does not fit the standard form in Eq. (24), the execution

16

error is conservatively approximated when constructing the convex subproblem. Since $\cos\left(2\pi w_\theta\right) \leq 1$, $\sin\left(2\pi w_\theta\right) \leq 1$, $\left|\sin\left(\sigma_p w_p\right)\right| \leq \sigma_p w_p$, $\cos\left(\sigma_p w_p\right) \leq 1$ (also, the latter two equalities hold approximately for small $\sigma_p w_p$), $g(\cdot)$ is conservatively modeled as:

$$g(\boldsymbol{x}, \boldsymbol{u}) = \|\boldsymbol{a}_s(\boldsymbol{x}, \boldsymbol{u})\|_2 \, {}^I\mathbf{C}_O(\boldsymbol{x}) T\left({}^O\boldsymbol{a}_s(\boldsymbol{x}, \boldsymbol{u})\right) \mathrm{diag}(\sigma_p, \sigma_p, \sigma_m), \tag{58}$$

where note that the quantity is converted to the I-frame by multiplying ${}^I\mathbf{C}_O(\boldsymbol{x})$. In the nonlinear Monte Carlo simulations, the original expression Eq. (56) is used with a sampling interval of one day.

The observation process is modeled as a simple linear system with additive noise, defined as:

$$\boldsymbol{f}_o(\boldsymbol{x}_k) = \boldsymbol{x}_k, \quad \boldsymbol{g}_o(\boldsymbol{x}_k) = \mathrm{blkdiag}(\sigma_r^{\mathrm{nav}} I_3, \sigma_v^{\mathrm{nav}} I_3), \tag{59}$$

where $\{\sigma_r^{\mathrm{nav}}, \sigma_v^{\mathrm{nav}}\}$ are the standard deviations of the position and velocity knowledge errors, representing OD errors. Their specific values are assumed to be $\{\sigma_r^{\mathrm{nav}}, \sigma_v^{\mathrm{nav}}\} = \{200 \text{ km}, 0.1 \text{ m/s}\}$ based on previous OD analysis. State knowledge updates (i.e., OD results) are assumed to be available at every ~13.3 days.

The cost function is formulated to minimize the nominal cumulative cone angle over the transfer. To be more specific, $\mathcal{L}_k = \sin\bar{\alpha}_k$ is used as the stage cost in Eq. (29).

Path chance constraints are imposed on the control inputs, formulated as:

$$\begin{aligned} &\mathbb{P}\left[\alpha_k \geq \alpha_{\min}\right] \geq 1 - \varepsilon_u, \quad \mathbb{P}\left[\alpha_k \leq \alpha_{\max}\right] \geq 1 - \varepsilon_u, \quad \mathbb{P}\left[\beta_k \geq -\pi\right] \geq 1 - \varepsilon_u, \quad \mathbb{P}\left[\beta_k \leq \pi\right] \geq 1 - \varepsilon_u, \\ &\mathbb{P}\left[|\alpha_k - \bar{\alpha}_k| \leq \tilde{\alpha}_{\max}\right] \geq 1 - \varepsilon_u, \quad \mathbb{P}\left[|\beta_k - \bar{\beta}_k| \leq \tilde{\beta}_{\max}\right] \geq 1 - \varepsilon_u, \quad \forall k, \end{aligned} \tag{60}$$

where $\{\tilde{\alpha}_{\max}, \tilde{\beta}_{\max}\}$ are the maximum variations of the attitude angles from their nominal values (while allowing the violation with probability ε_u). The primary purpose of the last two constraints is to preserve the linearization accuracy, as the convex subproblem relies on the linearization of SRP acceleration (Eq. (3)) with respect to $\boldsymbol{u}$ (i.e., these constraints are not something operationally required). This study uses $\{\tilde{\alpha}_{\max}, \tilde{\beta}_{\max}\} = \{10 \text{ deg}, 15 \text{ deg}\}$. For the cone angle constraint, $\{\alpha_{\min}, \alpha_{\max}\} = \{0, 50 \text{ deg}\}$. The risk bound ε_u are set $\varepsilon_u = 10^{-3}/6$ so that the control constraints are to be satisfied with a probability greater than or equal to 99.9% overall (there are six constraints in Eq. (60)).

The state history is not constrained in the form of path constraints, but is constrained by the terminal constraints as in Eq. (31) to ensure the successful rendezvous with the target with sufficient accuracy. x_f is defined by the ephemeris of 2020 GE at 400 days past the epoch. P_f is defined as: $P_f = \mathrm{blkdiag}(\sigma_{rf} I_3, \sigma_{vf} I_3)$, where $\{\sigma_{rf}, \sigma_{vf}\} = \{3.3 \times 10^4 \text{ km}, 50 \text{ m/s}\}$ are used in the numerical example.

With this problem setup, the robust solar-sail trajectory design problem is solved by applying the solution method based on stochastic optimal control and sequential convex programming. Each convex programming step was solved with ~50 seconds using CVX [40], and the overall convergence was achieved after about 300 iterations, where a large portion of the last half iterations were small steps slowly improving the optimality.

The optimized reference trajectory and control profile are shown in Figs. 7(a) and 7(b), respectively. For comparison, Fig. 7(b) also includes a deterministic optimal trajectory that was solved without the stochastic components and used as the initial guess for our robust trajectory optimization problem. This comparison indicates clear differences between the deterministic optimal and stochastic optimal results; the cone angle profile of the robust one is much smoother with moderate values overall, and the clock angle profile indicates less rapid decrease around 180-200 days past epoch.

To confirm the robustness of the designed reference trajectory and associated feedback policies, nonlinear Monte Carlo simulations are conducted with 1,000 samples, where the original nonlinear dynamics, control errors, and navigation errors are applied while the control updates are based on the linear (optimized) policies. The result is shown in Fig. 7(c) with its zoomed view around the arrival. For comparison, Fig. 7(d) shows the result of nonlinear Monte Carlo simulation *without* applying the trajectory corrections at all, signifying the necessity of having trajectory redesign process. These figures indicate that, under the optimized linear feedback policies, most of the trajectories are successfully rendezvousing with the asteroid within the prescribed covariance (shown as the 99.9% confidence ellipse in black) while some trajectories are missing the rendezvous. This discrepancy would be mainly due to the linearization accuracy on which the covariance propagation relies, implying that another means of verifying the robustness (e.g., performing nonlinear optimization of all the samples at every time step, like the one employed for the Dawn mission [41], which performs Monte Carlo low-thrust trajectory optimization using Mystic [28]) would be essential in order to conclude that the designed trajectory is indeed robust to all the considered uncertain errors.
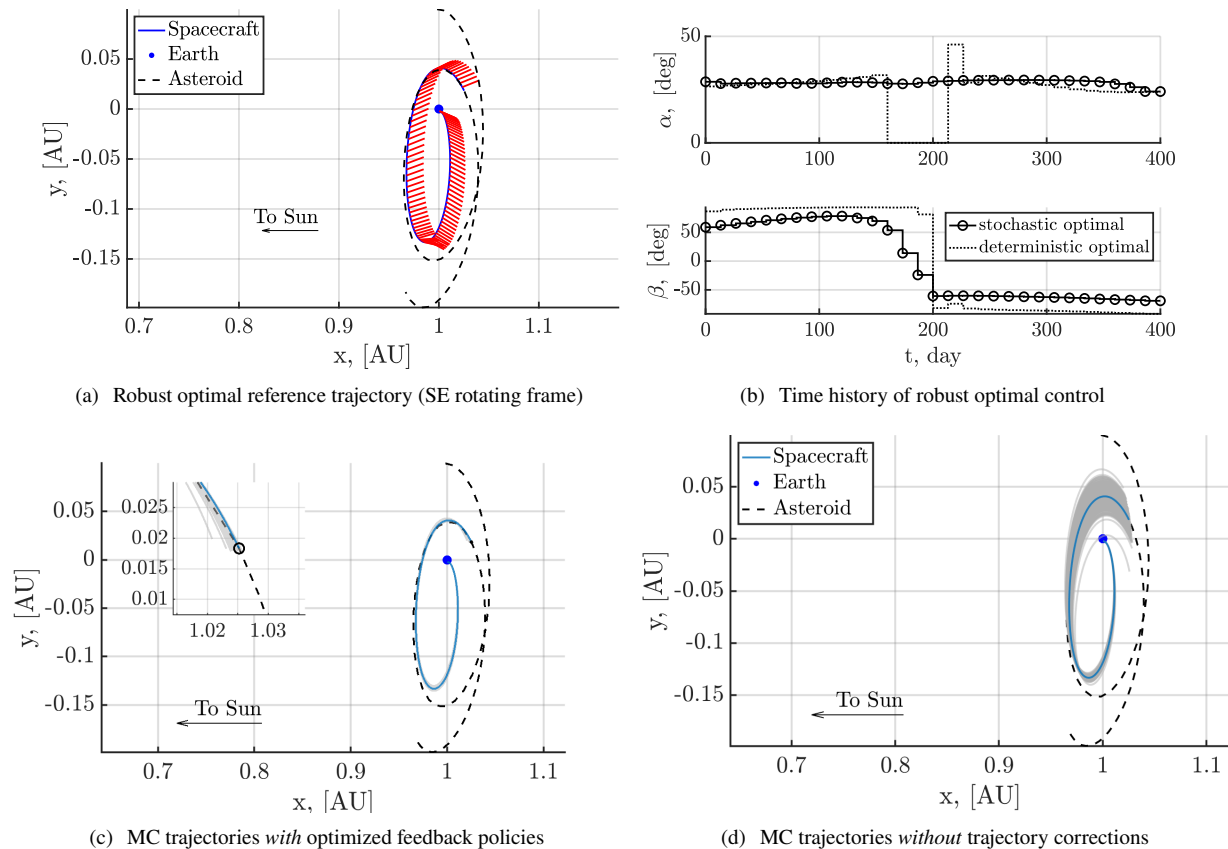
(a) Robust optimal reference trajectory (SE rotating frame)

(b) Time history of robust optimal control

(c) MC trajectories *with* optimized feedback policies

(d) MC trajectories *without* trajectory corrections

Figure 7   Robust sail trajectory to 2020 GE designed by stochastic optimal control and successive convexification

VII. Conclusions

This paper presents approaches to the design of robust solar-sail trajectories under uncertainty. Specifically, two distinct approaches, deterministic and stochastic approaches, are developed and applied to the mission design of the NEA Scout mission interplanetary cruise phase. The deterministic approach introduces a new set of objective metrics for solar sailing, derives their optimal control laws, and applies them to the design of reference trajectories with candidate mission margins identified in backward reachability analysis. The resilience of these trajectories against safe-mode events are evaluated and compared against the one without margins, confirming the enhanced robustness. The stochastic approach develops a solution method based on stochastic optimal control and sequential convex programming to design robust trajectories under navigation and control errors, which automatically introduces mission margins into reference trajectories. The future work includes further exploration of margin quantities for solar sailing to ensure the resilience against safe-mode events and formally verifying the robustness of the trajectories designed with the stochastic approach via Monte Carlo optimization of each sample trajectory.

Acknowledgments

References

[1] Tsuda, Y., Mori, O., Funase, R., Sawada, H., Yamamoto, T., Saiki, T., Endo, T., Yonekura, K., Hoshino, H., and Kawaguchi, J., "Achievement of IKAROS — Japanese deep space solar sail demonstration mission," *Acta Astronautica*, Vol. 82, No. 2, 2013, pp. 183–188. https://doi.org/10.1016/j.actaastro.2012.03.032.

[2] Johnson, L., Whorton, M., Heaton, A., Pinson, R., Laue, G., and Adams, C., "NanoSail-D: A solar sail demonstration mission," *Acta Astronautica*, Vol. 68, No. 5-6, 2011, pp. 571–575. https://doi.org/10.1016/j.actaastro.2010.02.008.

[3] Spencer, D. A., Betts, B., Bellardo, J. M., Diaz, A., Plante, B., and Mansell, J. R., "The LightSail 2 solar sailing technology demonstration," *Advances in Space Research*, Vol. 67, No. 9, 2021, pp. 2878–2889. https://doi.org/10.1016/j.asr.2020.06.029.

[4] Lockett, T. R., Castillo-Rogez, J., Johnson, L., Matus, J., Lightholder, J., Marinan, A., and Few, A., "Near-Earth Asteroid Scout Flight Mission," *IEEE Aerospace and Electronic Systems Magazine*, Vol. 35, No. 3, 2020, pp. 20–29. https://doi.org/10.1109/MAES.2019.2958729.

[5] Pezent, J. B., Sood, R., Heaton, A., Miller, K., and Johnson, L., "Preliminary trajectory design for NASA's Solar Cruiser: A technology demonstration mission," *Acta Astronautica*, Vol. 183, No. December 2020, 2021, pp. 134–140. https://doi.org/10.1016/j.actaastro.2021.03.006.

[6] Mori, O., Matsumoto, J., Chujo, T., Matsushita, M., Kato, H., Saiki, T., Tsuda, Y., Kawaguchi, J., Terui, F., Mimasu, Y., Ono, G., Ogawa, N., Takao, Y., Kubo, Y., Ohashi, K., Sugihara, A. K., Okada, T., Iwata, T., and Yano, H., "Solar power sail mission of OKEANOS," *Astrodynamics*, Vol. 4, No. 3, 2020, pp. 233–248. https://doi.org/10.1007/s42064-019-0067-8.

[7] WRIGHT, J., and WARMKE, J., "Solar sail mission applications," *Astrodynamics Conference*, American Institute of Aeronautics and Astronautics, Reston, Virigina, 1976. https://doi.org/10.2514/6.1976-808.

[8] SAUER, JR., C., "Optimum solar-sail interplanetary trajectories," *Astrodynamics Conference*, American Institute of Aeronautics and Astronautics, Reston, Virigina, 1976. https://doi.org/10.2514/6.1976-792.

[9] Ozimek, M. T., Grebow, D. J., and Howell, K. C., "Design of Solar Sail Trajectories with Applications to Lunar South Pole Coverage," *Journal of Guidance, Control, and Dynamics*, Vol. 32, No. 6, 2009, pp. 1884–1897. https://doi.org/10.2514/1.41963.

[10] Sood, R., and Howell, K., "Solar Sail Transfers and Trajectory Design to Sun-Earth L4, L5: Solar Observations and Potential Earth Trojan Exploration," *The Journal of the Astronautical Sciences*, Vol. 66, No. 3, 2019, pp. 247–281. https://doi.org/10.1007/s40295-018-00141-4.

[11] Mengali, G., Quarta, A. A., Circi, C., and Dachwald, B., "Refined Solar Sail Force Model with Mission Application," *Journal of Guidance, Control, and Dynamics*, Vol. 30, No. 2, 2007, pp. 512–520. https://doi.org/10.2514/1.24779.

[12] Oguri, K., Lantoine, G., and McMahon, J. W., "Solar Sailing Primer Vector Theory: Indirect Trajectory Optimization with Practical Mission Considerations," *Journal of Guidance, Control, and Dynamics*, 2021, pp. 1–9. https://doi.org/10.2514/1.G006210.

[13] Ozaki, N., Campagnola, S., and Funase, R., "Tube Stochastic Optimal Control for Nonlinear Constrained Trajectory Optimization Problems," *Journal of Guidance, Control, and Dynamics*, Vol. 43, No. 4, 2020, pp. 645–655. https://doi.org/10.2514/1.G004363.

[14] Greco, C., Di Carlo, M., Vasile, M., and Epenoy, R., "Direct multiple shooting transcription with polynomial algebra for optimal control problems under uncertainty," *Acta Astronautica*, Vol. 170, No. 5, 2020, pp. 224–234. https://doi.org/10.1016/j.actaastro.2019.12.010.

[15] Ridderhof, J., Pilipovsky, J., and Tsiotras, P., "Chance-constrained Covariance Control for Low-Thrust Minimum-Fuel Trajectory Optimization," *AAS/AIAA Astrodynamics Specialist Conference*, AAS, South Lake Tahoe, CA (Virtual), 2020.

[16] Oguri, K., and McMahon, J. W., "Stochastic Primer Vector for Robust Low-Thrust Trajectory Design Under Uncertainty," *Journal of Guidance, Control, and Dynamics*, 2021, pp. 1–19. https://doi.org/10.2514/1.G005970.

[17] Rios-Reyes, L., and Scheeres, D., "Robust Solar Sail Trajectory Control for Large Pre-Launch Modeling Errors," *AIAA Guidance, Navigation, and Control Conference and Exhibit*, Vol. 5, American Institute of Aeronautics and Astronautics, Reston, Virigina, 2005, pp. 3295–3312. https://doi.org/10.2514/6.2005-6173.

[18] Ozaki, N., Funase, R., Campagnola, S., and Yam, C. H., "Robust-Optimal Trajectory Design against Disturbance for Solar Sailing Spacecraft," *AIAA/AAS Astrodynamics Specialist Conference*, American Institute of Aeronautics and Astronautics, Reston, Virginia, 2016, pp. 1–19. https://doi.org/10.2514/6.2016-5578.

[19] Rubinsztejn, A., Sandel, C. G., Pezent, J. B., Sood, R., Laipert, F. E., Heaton, A., and Johnson, L., "Design of Solar Sailing Trajectories Resilient to Sate Mode Events," *AAS/AIAA Astrodynamics Specialist Conference*, 2021.

[20] McInnes, C. R., "Solar radiation pressure," *Solar Sailing: Technology, Dynamics and Mission Applications*, Springer-Verlag, Chichester, England, U.K., 1999, Chap. 2.

[21] Walker, M. J. H., Ireland, B., and Owens, J., "A set modified equinoctial orbit elements," *Celestial Mechanics*, Vol. 36, No. 4, 1985, pp. 409–419. https://doi.org/10.1007/BF01227493.

[22] Rayman, M. D., Fraschetti, T. C., Raymond, C. A., and Russell, C. T., "Coupling of system resource margins through the use of electric propulsion: Implications in preparing for the Dawn mission to Ceres and Vesta," *Acta Astronautica*, Vol. 60, No. 10-11, 2007, pp. 930–938. https://doi.org/10.1016/j.actaastro.2006.11.012.

[23] Oh, D., Landau, D., Randolph, T., Timmerman, P., Chase, J., Sims, J., and Kowalkowski, T., "Analysis of System Margins on Deep Space Missions Using Solar Electric Propulsion," *44th AIAA/ASME/SAE/ASEE Joint Propulsion Conference and Exhibit*, American Institute of Aeronautics and Astronautics, Reston, Virigina, 2008, pp. 1–30. https://doi.org/10.2514/6.2008-5286.

[24] Jehn, R., Schoenmaekers, J., Garc´ıa, D., and Ferri, P., "BepiColombo - Mission to mercury," *21st International Symposium on Space Flight Dynamics (ISSFD)*, Toulouse, France, 2009.

[25] Hart, W., Oh, D., Polanskey, C., Seal, D., Snyder, S., Stevens, S., and Trofimov, D., "A Margin Management Strategy for Low Thrust Trajectories on the Psyche Project," *2020 IEEE Aerospace Conference*, IEEE, 2020, pp. 1–16. https://doi.org/10.1109/AERO47225.2020.9172250.

[26] Mengali, G., and Quarta, A. A., "Optimal Three-Dimensional Interplanetary Rendezvous Using Non-Ideal Solar Sail," *Journal of Guidance, Control, and Dynamics*, Vol. 28, No. 1, 2005, pp. 173–177. https://doi.org/10.2514/1.8325.

[27] Dachwald, B., "Optimal Solar Sail Trajectories for Missions to the Outer Solar System," *Journal of Guidance, Control, and Dynamics*, Vol. 28, No. 6, 2005, pp. 1187–1193. https://doi.org/10.2514/1.13301.

[28] Whiffen, G., "Mystic: Implementation of the Static Dynamic Optimal Control Algorithm for High-Fidelity, Low-Thrust Trajectory Design," *AIAA/AAS Astrodynamics Specialist Conference and Exhibit*, Vol. 3, American Institute of Aeronautics and Astronautics, Reston, Virigina, 2006, pp. 1804–1815. https://doi.org/10.2514/6.2006-6741.

[29] Bryson, A. E., Ho, Y.-C., Bryson, A. E., and Ho, Y.-C., "Optimization problems for dynamic systems with path constraints," *Applied Optimal Control*, CRC Press, 2018, Chap. 3, pp. 90–127. https://doi.org/10.1201/9781315137667-3.

[30] Oguri, K., and McMahon, J. W., "Solar Radiation Pressure–Based Orbit Control with Application to Small-Body Landing," *Journal of Guidance, Control, and Dynamics*, Vol. 43, No. 2, 2020, pp. 195–211. https://doi.org/10.2514/1.G004489.

[31] Imken, T., Randolph, T., DiNicola, M., and Nicholas, A., "Modeling spacecraft safe mode events," *2018 IEEE Aerospace Conference*, Vol. 2018-March, IEEE, 2018, pp. 1–13. https://doi.org/10.1109/AERO.2018.8396383.

[32] Olympio, J. T., "Designing robust low-thrust interplanetary trajectories subject to one temporary engine failure," *AAS/AIAA Space Flight Mechanics Meeting*, San Diego, CA, 2010.

[33] Venigalla, C., Englander, J. A., and Scheeres, D. J., "Low-Thrust Trajectory Optimization for Maximum Missed Thrust Recovery Margin," *AAS/AIAA Astrodynamics Specialist Conference*, AAS, South Lake Tahoe, CA (Virtual), 2020.

[34] Rubinsztejn, A., Sandel, C. G., Sood, R., and Laipert, F. E., "Designing trajectories resilient to missed thrust events using expected thrust fraction," *Aerospace Science and Technology*, Vol. 115, 2021, p. 106780. https://doi.org/10.1016/j.ast.2021.106780.

[35] Laipert, F. E., and Longuski, J. M., "Automated Missed-Thrust Propellant Margin Analysis for Low-Thrust Trajectories," *Journal of Spacecraft and Rockets*, Vol. 52, No. 4, 2015, pp. 1135–1143. https://doi.org/10.2514/1.A33264.

[36] Ridderhof, J., Okamoto, K., and Tsiotras, P., "Chance Constrained Covariance Control for Linear Stochastic Systems With Output Feedback," *2020 59th IEEE Conference on Decision and Control (CDC)*, Vol. 2020-Decem, IEEE, 2020, pp. 1758–1763. https://doi.org/10.1109/CDC42340.2020.9303731.

[37] Mao, Y., Szmuk, M., and Acikmese, B., "Successive convexification of non-convex optimal control problems and its convergence properties," *2016 IEEE 55th Conference on Decision and Control (CDC)*, IEEE, 2016, pp. 3636–3641. https://doi.org/10.1109/CDC.2016.7798816.

[38] Mao, Y., Szmuk, M., Xu, X., and Acikmese, B., "Successive Convexification: A Superlinearly Convergent Algorithm for Non-convex Optimal Control Problems," *arXiv preprint*, 2018, pp. 1–35.

[39] Szmuk, M., Reynolds, T. P., and Açıkmeşe, B., "Successive Convexification for Real-Time Six-Degree-of-Freedom Powered Descent Guidance with State-Triggered Constraints," *Journal of Guidance, Control, and Dynamics*, Vol. 43, No. 8, 2020, pp. 1399–1413. https://doi.org/10.2514/1.G004549.

[40] Grant, M., and Boyd, S., "CVX: Matlab Software for Disciplined Convex Programming, version 2.1," , mar 2014.

[41] Parcher, D. W., and Whiffen, G. J., "Dawn statistical maneuver design for Vesta operations," *Advances in the Astronautical Sciences*, Vol. 140, 2011, pp. 1159–1176.